Cell Reports
Medicine

Article

Re-purposing the pro-senescence properties of doxorubicin to introduce immunotherapy in breast cancer brain metastasis

Graphical abstract

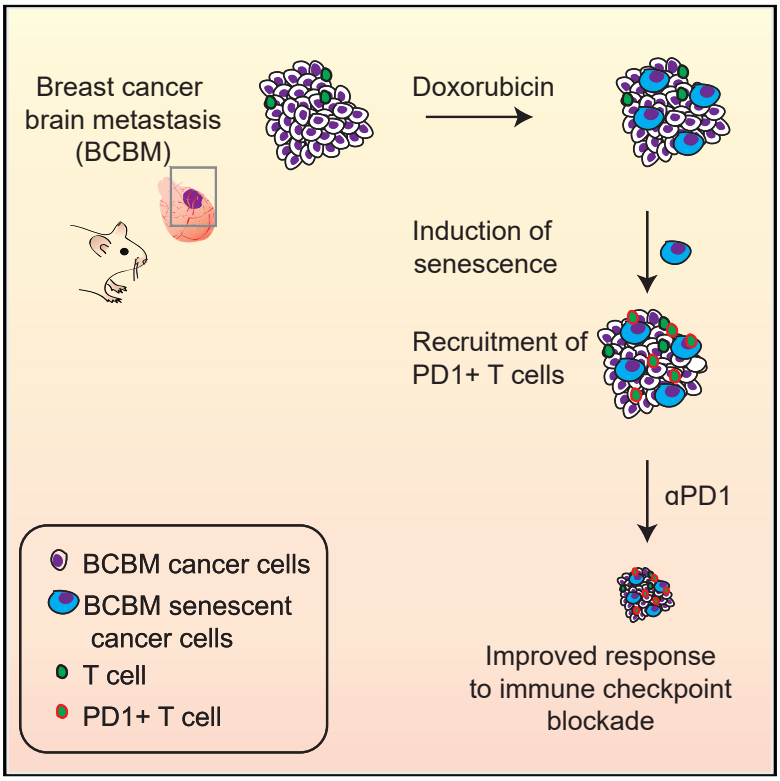

Highlights

- Generation of two mouse breast cancer brain metastasis (BCBM) models
- Doxorubicin induces a senescence program in BCBM
- Senescent cells in BCBM recruits PD1$^+$ T cells to BCBM
- Doxorubicin pre-treatment improves immune checkpoint blockade in BCBM

Authors

Rebeca Uceda-Castro, Andreia S. Margarido, Lesley Cornet, ..., Marike L.D. Broekman, Claire Vennin, Jacco van Rheenen

Correspondence

c.vennin@nki.nl (C.V.), j.v.rheenen@nki.nl (J.v.R.)

In brief

Uceda-Castro et al. generate two models of BCBM to optimize immunotherapy in this disease, which is considered untreatable. They demonstrate that doxorubicin induces senescence and in turn triggers a recruitment of PD1$^+$ T cells. Combining doxorubicin with anti-PD1 significantly improves survival, in a CD8$^+$ T cell-dependent manner.

Uceda-Castro et al., 2022, Cell Reports Medicine *3*, 100821
November 15, 2022
https://doi.org/10.1016/j.xcrm.2022.100821

CellPress

Cell Reports Medicine

CellPress
OPEN ACCESS

Article

Re-purposing the pro-senescence properties of doxorubicin to introduce immunotherapy in breast cancer brain metastasis

Rebeca Uceda-Castro,[1,14] Andreia S. Margarido,[1,14] Lesley Cornet,[1] Serena Vegna,[2] Kerstin Hahn,[1] Ji-Ying Song,[3] Diana A. Putavet,[4] Mariska van Geldorp,[5] Ceren H. Çitirikkaya,[5] Peter L.J. de Keizer,[4] Leon C. ter Beek,[6] Gerben R. Borst,[7,8,9] Leila Akkari,[2] Olaf van Tellingen,[5,10] Marike L.D. Broekman,[11,12,13] Claire Vennin,[1,*] and Jacco van Rheenen[1,15,*]

[1]Division of Molecular Pathology, Oncode Institute, The Netherlands Cancer Institute, 1066 Amsterdam, North Holland, the Netherlands
[2]Division of Tumor Biology and Immunology, Oncode Institute, The Netherlands Cancer Institute, 1066 Amsterdam, North Holland, the Netherlands
[3]Division of Experimental Animal Pathology, The Netherlands Cancer Institute, 1066 Amsterdam, North Holland, the Netherlands
[4]Center for Molecular Medicine, Division LAB, University Medical Center Utrecht, 3584 Utrecht, North Holland, the Netherlands
[5]Division of Pharmacology, The Netherlands Cancer Institute, 1066 Amsterdam, North Holland, the Netherlands
[6]Department of Medical Physics and Technology, The Netherlands Cancer Institute, 1066 Amsterdam, North Holland, the Netherlands
[7]Department of Radiation Oncology, The Netherlands Cancer Institute, 1066 Amsterdam, North Holland, the Netherlands
[8]Faculty of Biology, Medicine and Health, University of Manchester, Manchester M1 3WE, UK
[9]The Christie NHS Foundation Trust, Manchester M20 4BX, UK
[10]Mouse Cancer Clinic, the Netherlands Cancer Institute, 1066 Amsterdam, North Holland, the Netherlands
[11]Department of Neurosurgery, Leiden University Medical Center, 2300 Leiden, South-Holland, the Netherlands
[12]Department of Neurosurgery, Haaglanden Medical Center, Lijnbaan, 2597 The Hague, South-Holland, the Netherlands
[13]Department of Neurology, Massachusetts General Hospital, Harvard Medical School, Boston, MA 02115, USA
[14]These authors contributed equally
[15]Lead contact
*Correspondence: c.vennin@nki.nl (C.V.), j.v.rheenen@nki.nl (J.v.R.)
https://doi.org/10.1016/j.xcrm.2022.100821

SUMMARY

An increasing number of breast cancer patients develop brain metastases (BM). Standard-of-care treatments are largely inefficient, and breast cancer brain metastasis (BCBM) patients are considered untreatable. Immunotherapies are not successfully employed in BCBM, in part because breast cancer is a "cold" tumor and also because the brain tissue has a unique immune landscape. Here, we generate and characterize immunocompetent models of BCBM derived from PyMT and Neu mammary tumors to test how harnessing the pro-senescence properties of doxorubicin can be used to prime the specific immune BCBM microenvironment. We reveal that BCBM senescent cells, induced by doxorubicin, trigger the recruitment of PD1-expressing T cells to the brain. Importantly, we demonstrate that induction of senescence with doxorubicin improves the efficacy of immunotherapy with anti-PD1 in BCBM in a CD8 T cell-dependent manner, thereby providing an optimized strategy to introduce immune-based treatments in this lethal disease. In addition, our BCBM models can be used for pre-clinical testing of other therapeutic strategies in the future.

INTRODUCTION

Breast cancer brain metastasis (BCBM) is a leading cause of death for breast cancer (BC) patients. A recent meta-analysis has shown that for patients with metastatic BC, BCBM affects 31% of patients from the Her2$^+$ subtype, 32% of patients with triple-negative BC and 15% of patients with hormone receptor positive/Her2$^-$ disease, and their overall survival is dire.[1–3] Standard-of-care treatments for BCBM comprise systemic therapies with chemotherapies and targeted agents, radiotherapy, and neurosurgical resection. Additionally for Her2$^+$ BCBM patients, treatment with trastuzumab-deruxtecan has shown some clinical benefits.[4] However standard-of-care treatments are largely unsuccessful. This is in part due to the presence of the impermeable blood brain barrier (BBB) and the blood brain tumor barrier (BTB) as well as important resistance to chemotherapy and radiotherapy.[5] Consequently, survival of BCBM patients remains dreary and there is an urgent need to develop better, alternative therapeutic strategies for this disease.[1,2]

Immunotherapies have revolutionized cancer treatment in several solid tumor types[6–10]; however, only a limited number of clinical trials have explored the efficacy of immunotherapy in BC patients. In addition, BCBM patients have historically been excluded from those trials, due to the brain tissue that has long

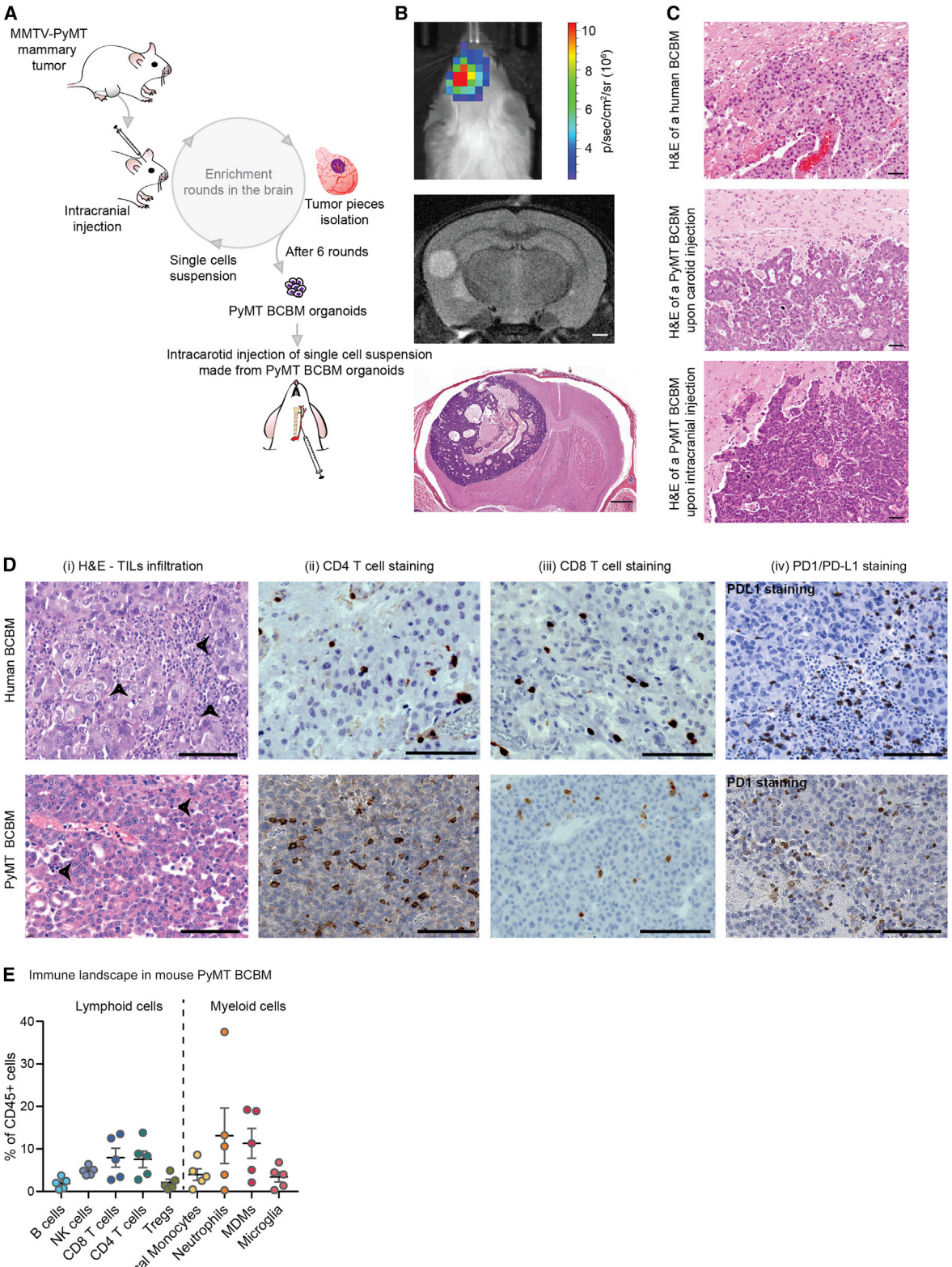

(legend on next page)

been depicted as an immune-privileged site.[11,12] However, specific immune reactions still occur in brain tumors and are commonly characterized by a high contribution of tumor-promoting myeloid cells, a low penetrance of cytotoxic T cells, and high T cell exhaustion, which hinder the efficacy of immunotherapies.[13,14] Recent findings in melanoma and lung BM have, however, challenged this view by demonstrating that some of those patients may benefit from immunotherapy.[6] Those encouraging findings are concomitant with the recent inclusion of BCBM patients in a number of clinical trials assessing the efficacy of immune-based treatments or other therapies.[15–17] Nevertheless, to date, nab-paclitaxel combined with anti-PD-L1 is the only strategy approved by the Food and Drug Administration for immunotherapy in triple-negative BCBM, but patients' response to the treatment remains limited.[15] Consequently, exploring new opportunities to prime the specific immune BCBM environment is required to introduce immunotherapy in this disease.

Several studies report attempts to render "cold" tumors more prone to respond to immunotherapies. For example, conventional chemotherapies can display immunomodulatory properties and influence immune responses. On the one hand, chemotherapies may modify the immune-properties of cancer cells, for instance by increasing cytokine production or provoking chromosomal instability or immunogenic cell death (reviewed in Galluzzi et al.[18] and Kersten et al.[19]). On the other hand, chemotherapies can also directly influence the properties of immune cells, such as regulatory T cells (Tregs), tumor-associated myeloid cells, or Natural Killer (NK) cells.[20–23] These findings have recently led to clinical applications, where the immunomodulatory properties of chemotherapies are exploited to recruit immune cells to tumor sites and to sensitize "cold" tumors to immunotherapies.[15,24–26]

In addition to killing cancer cells, chemotherapeutics can also induce a senescence state in the cancer cell population. Importantly, senescent cells are known to trigger a remodeling of the tumor microenvironment (TME) as well as of the tumor immune landscape via secretion of factors that belong to the senescence-associated secretory phenotype (SASP).[27,28] Multiple senescence phenotypes have been characterized and vary depending on the senescence-induction modalities. In addition, the effects of senescence and of the SASP on the immune TME are context- and tumor type-dependent.[29,30] However, the effects of chemotherapy-induced senescent cells on shaping the immune landscape of BCBM have not been assessed before.

The rareness of clinical trials in BCBM, the historical exclusion of BCBM patients from most immunotherapy trials,[1,5] and the scarcity of immunocompetent BCBM animal models limit the study of strategies to prime the specific immune microenvironment of BCBM. Here, we test whether inducing senescence in BCBM may be used to introduce immunotherapy in this disease. We used a PyMT BCBM pre-clinical mouse model, which harbors an intact immune system and recapitulates key immune features of human BCBM and we assessed the ability of doxorubicin to remodel the BCBM immune landscape. Doxorubicin is an anthracycline antibiotic that has been shown to induce senescence in a range of cancer types in a BMP4-Smad, p21 and p16-dependent manner.[31,32] In addition, liposomal-doxorubicin can cross the BBB and the BTB.[33–35] We demonstrate that inducing senescence with doxorubicin in BCBM tumor cells triggers a recruitment of PD1-expressing T cells to BCBM lesions, and this can be used to subsequently improve the efficacy of immunotherapy with anti-PD1. We confirm the efficacy of this therapeutic strategy in a second BCBM model derived from Neu mammary tumors. Together, we present evidence that chemotherapy-induced senescence renders BCBM sensitive to immunotherapy with checkpoint inhibitors, thereby opening new avenues for improved clinical management of this dreadful disease.

RESULTS

Generation and characterization of a PyMT BCBM model

In order to identify new approaches to render BCBM sensitive to immunotherapy, we used a mouse BCBM model generated via serial intracranial transplantations and carotid injections in immunocompetent Friend Virus B (FVB/NRj) inbred mice of tumor pieces derived from MMTV-PyMT mice that carry an E-cadherin-mCFP transgene[36] (see STAR Methods and Figure 1A and Margarido et al.[37]). Following six rounds of enrichment in the brain, we generated organoids from the BCBM and we engineered them with H2B-Dendra2 and luciferase constructs for imaging purposes (from herein referred to as "PyMT BCBM organoids"). Organoids are self-assembling miniature organ-like 3D *in vitro* structures that recapitulate with a high fidelity features of *in vivo* tumors such as cellular heterogeneity,[38] and which can be manipulated *in vitro* to express, for instance, fluorescent reporters. Tumor organoids have recently been used to accurately model cancer biology and to perform *in vitro* pre-clinical testings.[39] The PyMT BCBM organoids were cultured in 3D basal membrane extract (BME) matrices to avoid inducing

Figure 1. The mouse PyMT BCBM mimics immune features of the human disease

(A) Schematic representation of the generation of the mouse PyMT BCBM model.

(B) Representative images of a metastasis formation upon carotid injection. PyMT BCBM organoids were made as single cells just before injection in the carotid. Metastasis formation was confirmed by bioluminescence (top), MRI (medium), and H&E staining (bottom). Scale bar, 1 mm. Thirteen mice were injected in the carotid, and three developed a BCBM.

(C) Representative images of H&E staining of human BCBM (top) and of mouse PyMT BCBMs generated upon carotid (middle) and intracranial (bottom) injections of PyMT BCBM organoids. Scale bar, 50 μm.

(D) Representative images of H&E and immunohistochemistry staining for CD4, CD8, and PD-L1/PD1 in human (top) and PyMT BCBM derived from intracranial injection (bottom). On H&E images, black arrows point to tumor infiltrated lymphocytes (TILs). Scale bar, 100 μm.

(E) Quantification of immune cell populations infiltrated into the mouse BCBM, as assessed by flow cytometry. n = 5 mice, data are presented as averaged percentage cells out of $CD45^+$ immune cells.

See also Figures S1–S3.

artificially high metastatic properties that may arise upon 2D culturing.[40] We dissociated the PyMT BCBM organoids into single cells and injected them in the mouse carotid. In this context, the brain-enriched tumor cells were able to extravasate and to survive as single cells in the brain or to form BCBM in 3 out of 13 mice. This moderate metastatic efficiency is in line with a fairly sporadic spread to the brain in patients with metastatic breast cancer but demonstrates the ability of the PyMT BCBM organoids to home in this organ (Figure 1B). Intracranial injections of the PyMT BCBM organoids led to a humane end point of 33 days, providing a time window for therapeutic testing in contrast to other models that often cause death within 2 to 3 weeks after injection. Although these characteristics are required for pre-clinical studies like ours, a large number of animals is needed to study early BCBM formation.

Upon intracranial transplantations of the PyMT BCBM organoids, we observed BCBM formation in 100% of the mice. We monitored BCBM progression upon intracranial and carotid injections by IVIS imaging in a small cohort of mice (Figures S1A and S1B). Although a number of other BCBM models have been reported to develop in the brain dura,[41] the PyMT BCBM was found to grow in the brain parenchyma upon carotid injection (Figure S1C). In addition, multiple lesions of various sizes were found in the brain of mice injected in the carotid at humane endpoint; however, we cannot exclude that large metastases result from the fusion of multiple smaller metastases (Figure S1C). Moreover, injection of PyMT BCBM organoids into the carotid resulted in the development of metastasis in the abdominal cavity near the uterus horn and in the spleen in 1 out of 13 mice (Figure S1D). Histological assessments demonstrated that BCBMs that are formed upon carotid or intracranial transplantations display similar histopathological features (Figure 1C). Furthermore, mice that developed BCBM upon carotid injection had a mean survival of 70 days compared with 33 days for mice injected intracranially (Figure S1E).

In order to test whether the immune landscape evolves naturally in PyMT BCBM derived from intracranial injections, we compared immune infiltrates in PyMT BCBM derived from carotid versus intracranial injections using immunohistochemistry analyses. We did not find significant differences in cell number and tissue distribution of CD4 T cells, CD8 T cells, macrophages (F4/80), neutrophils (Ly6G), and regulatory T cells (Tregs, Foxp3) (Figure S2A). In addition, we did not observe significant differences in the number of PD1 expressing cells in BCBMs generated by both procedures (Figure S2A). Therefore, considering the similarities between PyMT BCBMs derived from intracranial and intracarotid injections and for improved experimental reproducibility and standardization, we used intracranial injections of PyMT BCBM organoids derived from the sixth round of enrichment for the rest of our study.

We next tested whether our mouse model of PyMT BCBM recapitulates features of the human disease. Immunohistopathological analyses demonstrated that the PyMT mouse BCBM resembled the human counterpart (see STAR Methods, Figures 1C and S2B). In addition, magnetic resonance imaging (MRI) and spectroscopy (MRS) confirmed that the mouse BCBM model mimics features of human brain metastasis (Figures S2C and S2D and STAR Methods).[42,43] Next, we performed immunohistochemical analyses of immune cell infiltration in human BCBM. Tumor-infiltrating lymphocytes (TILs, arrows), CD4 and CD8 T cells, as well as cells expressing PDL1 were observed in human BCBM sections (Figure 1D, top panel). High TILs content and PD-L1 expression are prognostic markers for good response to immunotherapy,[44] consequently this suggests that human BCBM may be targeted with immune-based treatments such as checkpoint inhibitors. Importantly, TILs, T cells, and PD1-positive cells were also found to infiltrate the mouse PyMT BCBM (Figure 1D, lower panel); however, it is unknown whether the level of PD1 positive T cell infiltration is sufficient to elicit a response to immune checkpoint blockade. We next mapped the immune landscape of the mouse PyMT BCBM derived from intracranial injections using flow cytometry (see Figure S3 for gating strategies). The mouse PyMT BCBM was infiltrated with immune cells of myeloid origin (neutrophils, monocytes, microglia, monocyte-derived macrophages [MDMs]), as well as lymphoid cells such as T and B cells (Figure 1E). This is in line with previously published work in human BCBM[13,45,46] and warrants the use of the PyMT BCBM mouse model for designing innovative strategies for immunotherapies in this disease.

Doxorubicin induces senescence in BCBM tumor cells

We next investigated whether doxorubicin can trigger senescence in BCBM. Doxorubicin is an anthracycline antibiotic, which has been shown to induce senescence in a variety of cell lines both *in vitro* and *in vivo*.[32] First, we treated PyMT BCBM organoids with low-dose doxorubicin (10 nmol/L) for 7 days *in vitro*. Over the course of the treatment, control-treated organoids continuously grew while doxorubicin-treated organoids remained small (Figure 2A). Treatment with low-dose doxorubicin led to a minor, non-statistically significant increase of apoptosis (Figure 2B), suggesting that other mechanisms may cause the stalling of organoid growth. Indeed, the expression of the senescence-related genes *CDKN2A* and *FOXO4*[47] was enhanced while the expression of the proliferative marker *Ki67* was reduced (Figure 2C). Next, PyMT BCBM organoids were intracranially injected into recipient FVB/NRj mice. Upon BCBM formation, as assessed by IVIS imaging, mice were administered three times with a saline vehicle or with doxorubicin (5 mg/kg) every 5 days (Figure 2D). In this context, *in vivo* treatment with doxorubicin induced an increase of senescence-associated (SA) β-Galactosidase activity in BCBM lesions compared with vehicle (Figure 2E), while the loss of lamin B1, a feature of senescent cells,[48–50] was also observed (Figure S4A) upon *in vivo* treatment with doxorubicin. In addition, the number of apoptotic BCBM cells was non-statistically significantly increased upon doxorubicin treatment compared with vehicle *in vivo* (Figure S4B). Together, this demonstrates that doxorubicin treatment correlates with the induction of a senescence program in our PyMT BCBM model both in *in vitro* organoids and *in vivo*.

Doxorubicin reshapes the immune landscape of BCBM

Using the immunomodulatory properties of chemotherapy is emerging as a potent strategy to increase immune infiltration into otherwise "cold" tumors.[19,51] In addition, senescent cells can remodel their environment via secretion of SASP factors.[27]

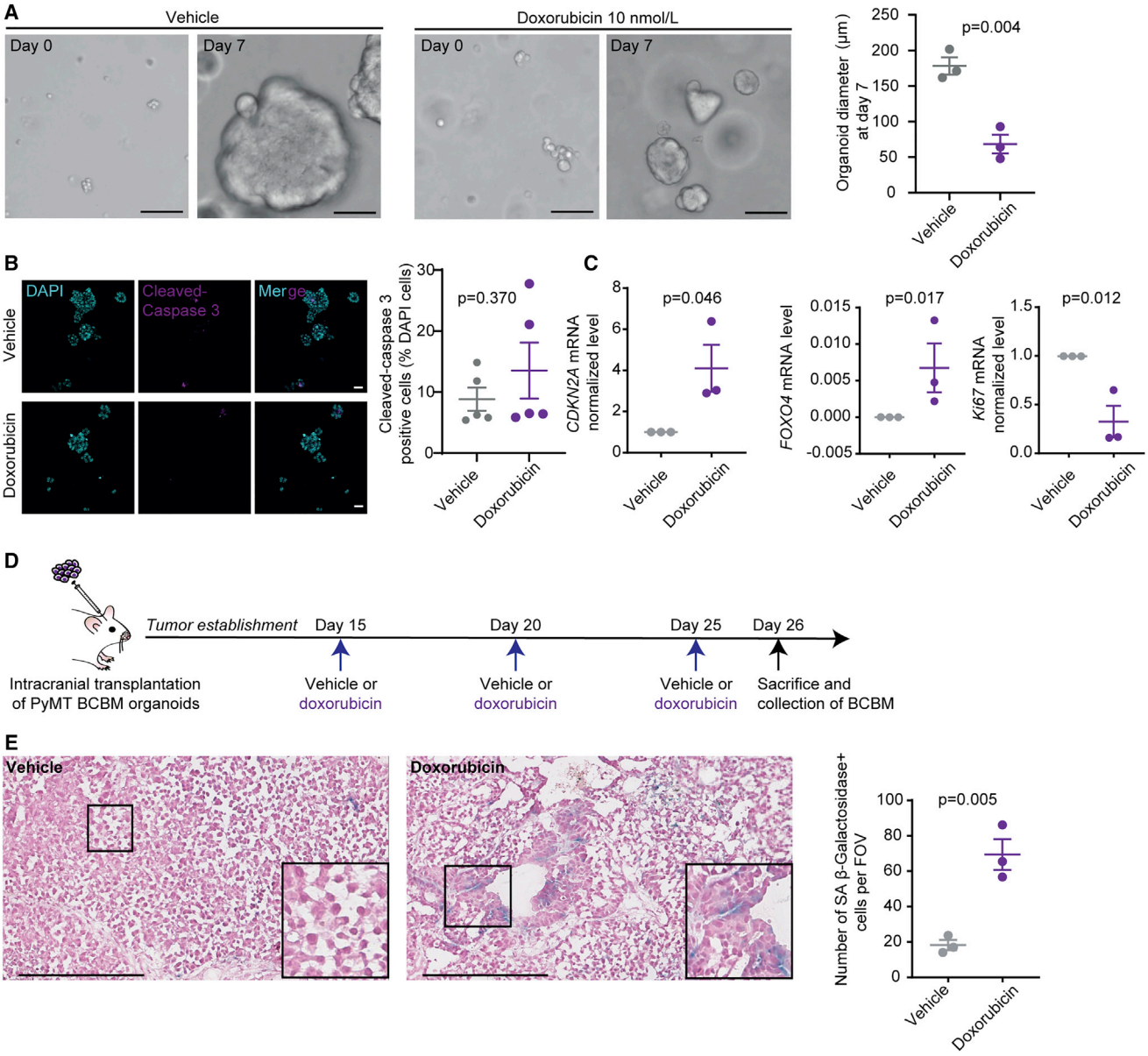

Figure 2. Doxorubicin induces senescence in PyMT BCBM

(A) Representative images of PyMT BCBM organoids and quantification of organoid diameter after 7 days of treatment with vehicle (saline) or with doxorubicin (10 nmol/L), n = 3 biological repeats with three technical replicates per repeat. Data are presented as mean ± SEM. Scale bar, 50 μm.

(B) Representative images and quantification of cleaved-caspase 3 immunofluorescent staining in mouse BCBM organoids treated with vehicle (saline) or with doxorubicin (10 nmol/L) for 7 days. n = 5 biological repeats. Data are presented as mean ± SEM. Scale bar, 50 μm.

(C) RT-qPCR analysis of CDKN2A, FOXO4, and Ki67 mRNA levels normalized to GAPDH in PyMT BCBM organoids treated with vehicle (saline) or doxorubicin (10 nmol/L) for 7 days. n = 3 biological repeats with three technical replicates per repeat. Data are presented as mean ± SEM.

(D) Schematic representation of experimental design and treatment timeline.

(E) Representative images and quantification of SA β-Galactosidase staining in *in vivo* PyMT BCBM treated with vehicle (saline) or with doxorubicin. n = 3 mice per group, with five fields of view analyzed and averaged per mouse. Data are presented as mean ± SEM. Scale bar, 200 μm.

See also Figure S4.

We therefore next assessed the effects of doxorubicin on the immune landscape of the PyMT BCBM model. Mice bearing BCBM were subjected to the same treatment with doxorubicin or vehicle as before (Figure 2D). To map the effects of doxorubicin on the PyMT BCBM immune landscape, mice were killed 24 h after the last treatment, and BCBM lesions were collected for analyses. Flow cytometry analyses revealed an increased infiltration of CD4 and CD8 T cells to BCBMs grown in mice treated

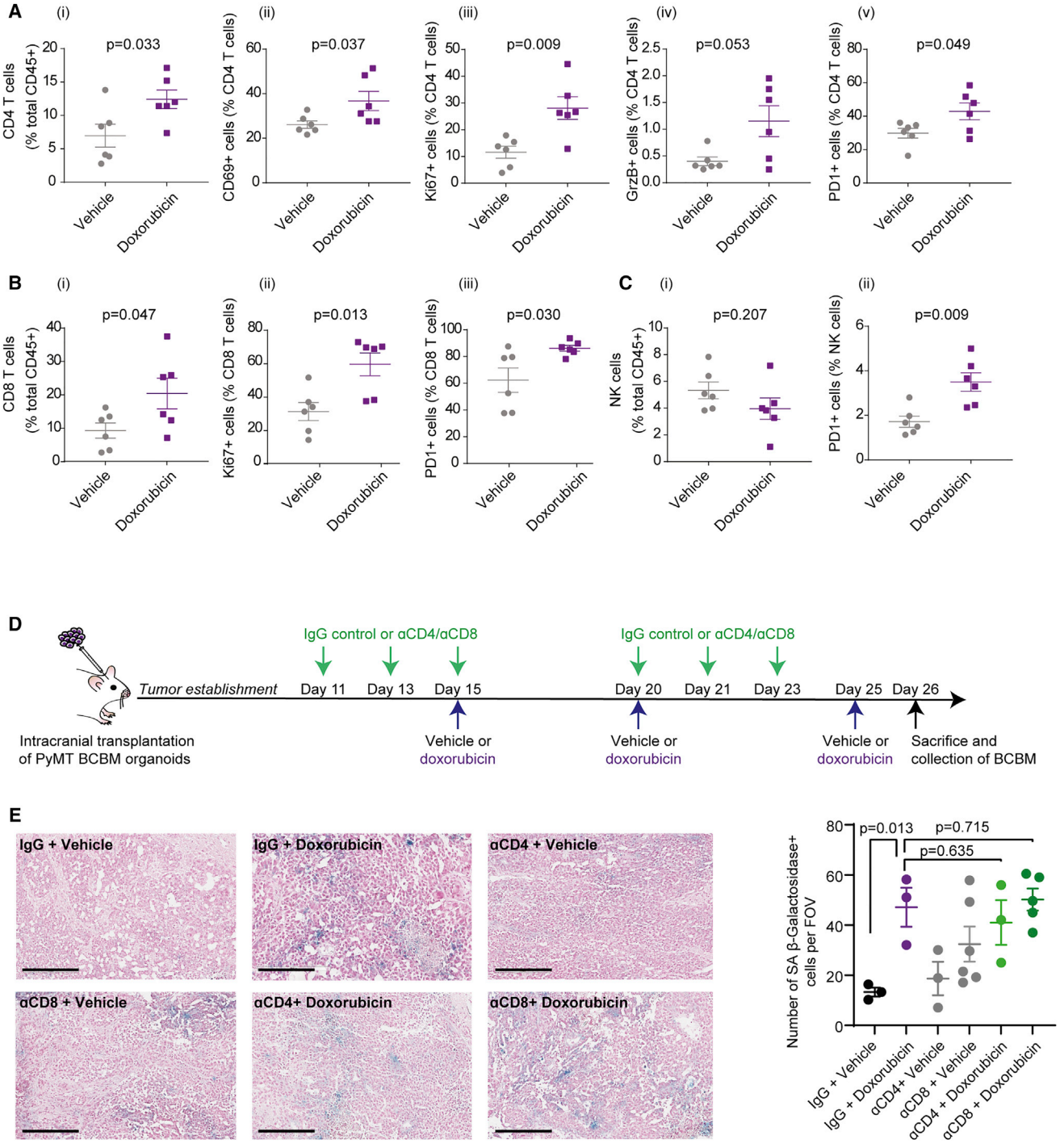

Figure 3. Doxorubicin reshapes the immune landscape in PyMT BCBM, yet recruited T cells do not clear senescent cancer cells

(A) Quantification of CD4 T cells as a percentage of $CD45^+$ cells (i), $CD69^+$ cells as a percentage of CD4 T cells (ii), $Ki67^+$ cells as a percentage of CD4 T cells (iii), Granzyme-B^+ cells as a percentage of CD4 T cells (iv), and $PD1^+$ cells as a percentage of CD4 T cells (v) infiltrated in PyMT BCBM upon treatment with vehicle (saline) or with doxorubicin. CD4 T cells were gated as $CD45^+/CD11b^-/NK1.1^-/CD19^-/CD4^+$ cells. Also see Figure S3A for gating strategy.

(B) Quantification of CD8 T cells as a percentage of $CD45^+$ cells (i), $Ki67^+$ cells as a percentage of CD8 T cells (ii), and $PD1^+$ cells as a percentage of CD8 T cells (iii) infiltrated in PyMT BCBM upon treatment with vehicle (saline) or with doxorubicin. CD8 T cells were gated as $CD45^+/CD11b^-/NK1.1^-/CD19^-/CD8^+$ cells. Also see Figure S3A for gating strategy.

(legend continued on next page)

with doxorubicin compared with vehicle (Figures 3A (i) and 3B (i)). Immunofluorescence analyses confirmed that infiltration of CD4 and CD8 T cells was increased in PyMT BCBMs upon treatment with doxorubicin (Figures S5A and S5B). Activated CD4 T cells expressing CD69, Ki67, and Granzyme-B as well as CD8 T cells expressing Ki67 were also found to be more abundant in PyMT BCBMs upon treatment with doxorubicin (Figures 3A (ii-iv) and 3B (ii)). Lastly, treatment with doxorubicin induced an increased infiltration of CD4 T cells, CD8 T cells, and NK cells expressing PD1 (Figures 3A (v), 3B (iii), and 3C). We observed minor, non-statistically significant differences for the content of B cells, Tregs, neutrophils, macrophages, and monocytes upon treatment with doxorubicin (Figures S5C and S5D).

Senescent cells are not cleared by infiltrated T cells upon chemotherapy

Intricate crosstalk between immune cells and senescent cells can direct the fate of either populations,[52–54] for instance immune cells may be recruited to clear senescent cells from aging or cancerous tissues.[55] Considering the increased infiltration of T cells upon doxorubicin, we next investigated whether T cell recruitment to PyMT BCBM led to clearance of senescent cells. Mice bearing PyMT BCBM were treated with vehicle or with doxorubicin, in combination with an immunoglobulin (Ig)G control or with depleting antibodies against CD4 or CD8, as previously described[56] (Figure 3D). Successful depletion of CD4 and CD8 cells in the PyMT BCBM was confirmed by immunohistochemistry (Figures S5E and S5F). In line with previous work showing that CD8 T cells can clear senescent cells,[55] depleting CD8 T cells in vehicle-treated mice increased the number of SA β-Galactosidase-positive cells (Figure 3E). However, the number of senescent cells in doxorubicin-treated mice administered with depleting antibodies against CD4 or CD8 was not significantly different than for doxorubicin-treated mice that received the IgG control (Figure 3E, compare purple with greens). This indicates that the recruitment of T cells to the PyMT BCBM upon doxorubicin treatment does not lead to clearance of senescent cells in our settings.

Senescent cells drive the recruitment of T cells to the BCBM without altering the tumor vasculature

We next assessed whether doxorubicin-induced senescent cells are involved in the recruitment of T cells to the PyMT BCBM. We used ABT263, a potent senolytic BH3 mimetic drug that inhibits the anti-apoptotic proteins BCL-2 and BCL-xL and that has been recently used to selectively ablate senescent cells in p53 proficient cellular models.[57,58] Small molecule Bcl-2 inhibitors have previously been used to successfully deplete senescent cells in primary and metastatic brain tumors in pre-clinical rodent models, demonstrating their ability to pass the BTB.[59–61] *In vitro*, treatment with ABT263 for 48 h induced cell death specifically in organoids pre-treated with low-dose doxorubicin for 7 days (Figures S6A and S6B). Moreover, to test whether ABT263 kills senescent cells, we generated a cell line from the PyMT BCBM organoids to perform an SA β-Galactosidase assay. In this setting, while doxorubicin significantly increased SA β-Galactosidase activity in PyMT BCBM cells, the population of SA β-Galactosidase$^+$ cells was ablated in BCBM cells treated with doxorubicin followed by ABT263, confirming the elimination of senescent cells by this senolytic agent (Figure S6C). Next, we tested the ability of ABT263 to deplete senescent cells *in vivo* (Figure 4A). Administration of ABT263 did not alter tumor progression (Figure S6D). Tumor cell morphology and tumor size were not significantly altered; however, we observed a mild reduction of necrosis and of inflammation upon treatment with ABT263 compared with vehicle (Figure S6E). Importantly, treatment with ABT263 in mice bearing PyMT BCBM reverted the increase of SA β-Galactosidase activity induced by doxorubicin, to a similar level as control conditions (Figure 4B), confirming the activity and specificity of this senolytic agent against senescent cells in our PyMT BCBM model.

Next, we tested whether clearance of senescent cells with ABT263 would affect the recruitment of T cells to the PyMT BCBM. Quantification of immunofluorescent staining for CD4 and CD8 in *in vivo* PyMT BCBM revealed that the recruitment of T cells to the BCBM triggered by doxorubicin treatment is reverted upon treatment with ABT263 (Figures 4C and 4D). To control for a potential direct effect of ABT263 on T cell behavior, we isolated T cells from the mouse spleen and treated them *in vitro* with DMSO or ABT263. We found neither significant differences in T cell proliferation nor alterations in their migrating capability upon treatment with ABT263 compared with DMSO (Figures S6F and S6G and Videos S1 and S2), confirming that the observed reduction in T cell recruitment to the BCBM upon ABT263 is not due to a direct effect of the senolytic agent on T cell viability or migration.

Lastly, induction of senescence can lead to a remodeling of the tumor vasculature, which has been shown to participate in the recruitment of T cells to the tumor mass.[28] We therefore evaluated whether doxorubicin triggered a remodeling of the BCBM vasculature. While we did not observe changes in blood vessel content in PyMT BCBM upon treatment with doxorubicin compared with vehicle (Figure S7A), we found higher levels of α-smooth muscle actin (αSMA) expression in the blood vessels of doxorubicin-treated BCBM compared with vehicle (Figure S7B). However we neither detected statistically significant changes in pericyte (NG2$^+$ cells) recruitment close to the vasculature (Figure S7C) nor statistically significant alterations of the

(C) Quantification of NK cells as a percentage of CD45$^+$ cells (i) and PD1$^+$ cells as percentage of NK cells (ii) infiltrated in PyMT BCBM upon treatment with vehicle (saline) or with doxorubicin. NK cells were gated as CD45$^+$/CD11b$^-$/NK1.1$^+$ cells. Please also see Figure S3A for gating strategy. For (A)–(C), data are presented as mean ± SEM, n = 6 mice per group.

(D) Schematic representation of experimental design and treatment timeline.

(E) Representative images and quantification of SA β-Galactosidase staining in PyMT BCBM treated with control IgG or depleting antibodies against CD4 or CD8 T cells, prior to treatment with vehicle (saline) or with doxorubicin. n = 3 mice for all groups expect for anti-CD8 followed by control with n = 6 mice and anti-CD8 followed by doxorubicin with n = 5 mice. Data are presented as mean ± SEM. Scale bar, 200 μm.

See also Figure S5.

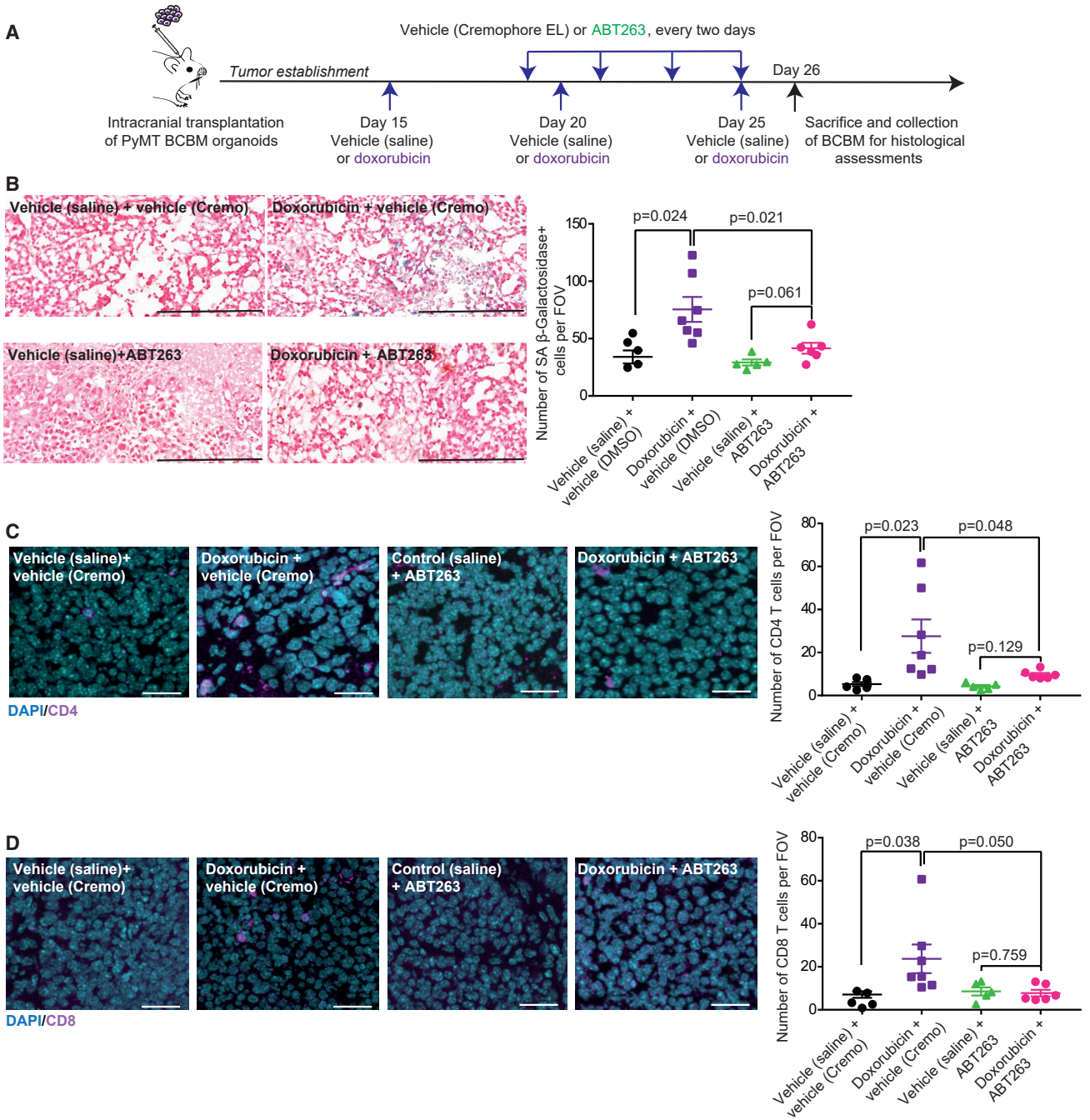

Figure 4. Senescent cells drive the recruitment of T cells to PyMT BCBM

(A) Schematic representation of experimental design and treatment timeline.

(B) Representative images and quantification of SA β-Galactosidase staining in *in vivo* PyMT BCBM upon treatment with vehicle (saline) and with a chromophore vehicle (n = 5 mice), doxorubicin and a chromophore vehicle (n = 7 mice), vehicle (saline) and ABT263 (n = 5 mice), or doxorubicin and ABT263 (n = 6 mice). Data are presented as mean ± SEM. Scale bar, 200 μm.

(C and D) Representative images and quantification of immunofluorescence staining for CD4 and (D) for CD8 upon treatment with vehicle (saline) and a chromophore vehicle (n = 5 mice), doxorubicin and a chromophore vehicle (n = 7 mice), vehicle (saline) and ABT263 (n = 5 mice) or doxorubicin and ABT263 (n = 6 mice). Data are presented as mean ± SEM. Scale bar, 100 μm.

See also Figures S6 and S7.

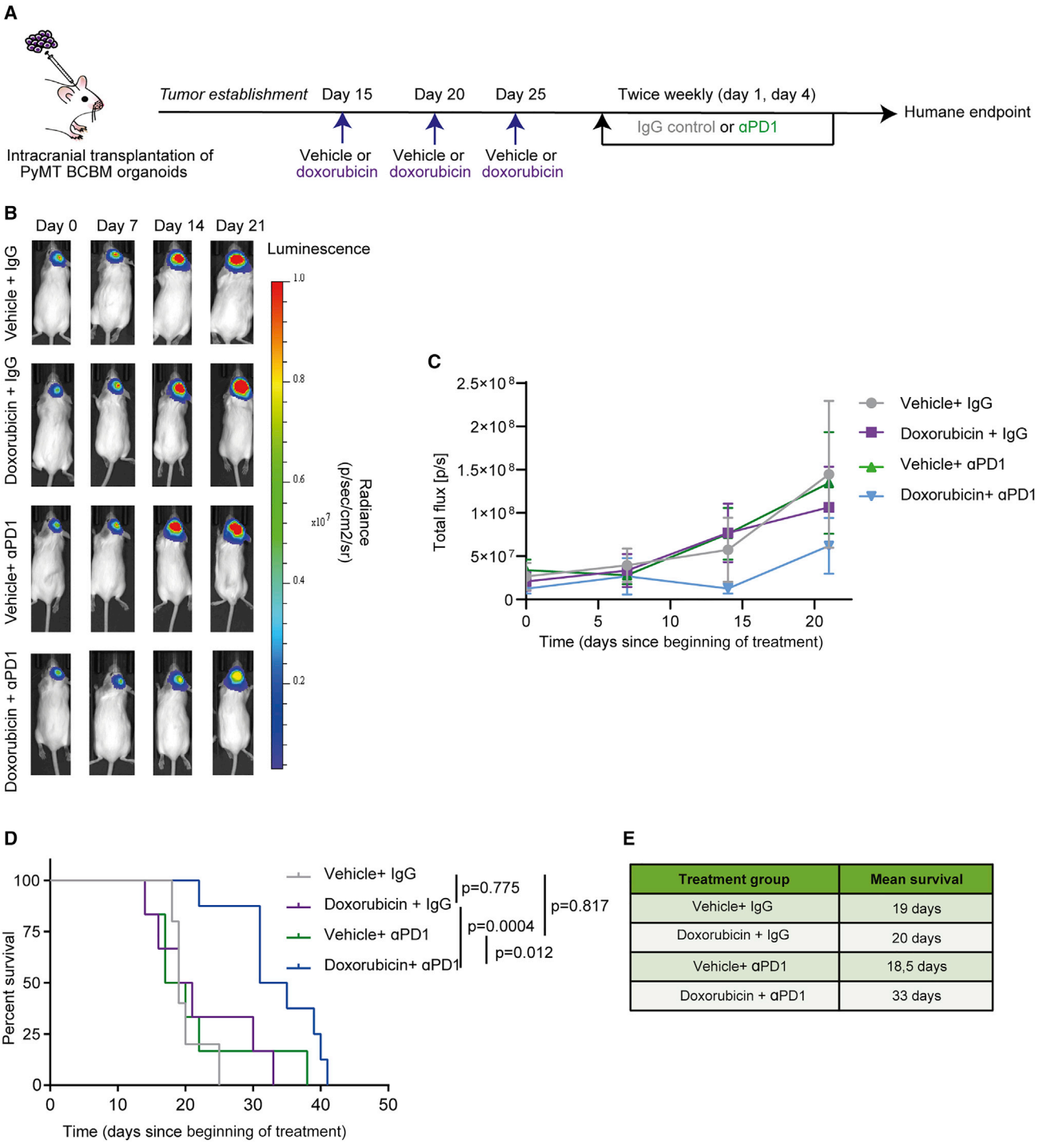

Treatment group	Mean survival
Vehicle+ IgG	19 days
Doxorubicin + IgG	20 days
Vehicle+ αPD1	18,5 days
Doxorubicin + αPD1	33 days

Figure 5. Pre-induction of senescence with doxorubicin improves the efficacy of anti-PD1

(A) Schematic representation of experimental design and treatment timeline. Upon establishment of BCBM, mice were randomized into treatment groups based on IVIS measurements and monitored using whole-body bioluminescence imaging until reaching humane endpoint.

(B) Representative images of whole-body IVIS bioluminescence monitoring of BCBM response to treatment. For each treatment group, images of a representative mouse followed over time from the beginning of the treatment (day 0) are depicted.

(C) IVIS bioluminescence flux averaged signal since the beginning of treatment in mice bearing BCBM and treated with vehicle (saline) followed by IgG control (n = 5 mice); pre-treatment with vehicle (saline) followed by anti-PD1 antibody (n = 6 mice); pre-treatment with doxorubicin followed by IgG (n = 6 mice); or pre-treatment with doxorubicin followed by anti-PD1 antibody (n = 8 mice).

(legend continued on next page)

expression levels of ICAM nor VCAM in the endothelial cells, two immunomodulatory cell surface molecules that have been linked with tissue inflammation and immune cell recruitment[62] (Figures S7D and S7E).

Together, this demonstrates the role of doxorubicin-induced senescent cells in re-shaping the BCBM immune landscape and driving the recruitment of T cells to the BCBM, without significantly altering features of the BTB at the studied timepoint.

Inducing senescence in BCBM improves the efficacy of anti-PD1

The presence of intratumoral PD1-positive T cells is commonly used as a prognostic marker of good response to immune checkpoint inhibition with anti-PD1.[44] In addition, the observed recruitment of PD1-positive T cells to the mouse PyMT BCBM triggered by doxorubicin is in line with observations reported for extracranial breast tumors in the TONIC trial.[51] This prompted us to test whether recruiting PD1-positive T cells to the PyMT BCBM via doxorubicin treatment could be used to improve anti-PD1 efficacy. To test this, FVB/NRj mice bearing PyMT BCBM received three administrations of vehicle or doxorubicin, prior to continuous treatment with an IgG control or with an anti-PD1 antibody, twice weekly (Figure 5A). Tumor response to treatments was monitored using whole-body bioluminescent imaging (Figures 5B and 5C), and mice were sacrificed when they showed signs of sickness. Doxorubicin treatment alone and anti-PD1 treatment alone neither significantly altered BCBM growth nor improved mouse survival compared with vehicle treatment (Figures 5B–5D), in line with the lack of induction of apoptosis by doxorubicin in the PyMT BCBM (Figure S4B) and with the poor response to monotherapies reported in BCBM patients.[1] However, pre-treatment with doxorubicin prior to PD1 blockade altered tumor growth and significantly prolonged mouse survival compared with vehicle and with single treatment with either doxorubicin or anti-PD1 (Figures 5B–5D). Mean survivals for each treatment group are depicted in Figure 5E.

Next, we evaluated whether the T cells that are recruited to the PyMT BCBM following doxorubicin treatment (Figure 3) underly the improved survival upon anti-PD1 therapy. We first studied CD44 expression, a marker of mature T cells,[63] in intratumoral T cells. The percentage of T cells that express CD44 was increased in the PyMT BCBM of mice treated with the combined treatment compared with monotherapies (Figures 6A and 6B), suggesting that T cells found in the PyMT BCBM have potent anti-tumor activity upon treatment with doxorubicin followed by anti-PD1. Notably, the percentage of CD8 T cells positive for CD44 was significantly higher compared with the CD4 T cells in this treatment group (Figures 6A and 6B). We then functionally tested the role of T cells in driving the response to anti-PD1 upon doxorubicin using depleting antibodies. Following pre-treatment with doxorubicin, mice bearing PyMT BCBM were continuously treated with IgG control or with depleting antibodies against CD4 or CD8, in combination with IgG control or anti-PD1 antibody twice weekly (as depicted in Figure 6C). Mice were sacrificed when symptomatic, as previously (Figure 5). Depleting CD8 cells significantly reduced mouse survival in response to doxorubicin followed by anti-PD1, while CD4-depletion did not (Figure 6D). Considering that doxorubicin also induces a recruitment of $PD1^+$ NK cells to the BCBM (Figure 3C (ii)), and in light of previous work indicating that NK cells can express CD8,[64] we next evaluated the percentage of the $PD1^+$ NK cell population that also expresses CD8. We found that out of the total $CD45^+$ cells in the PyMT BCBM, only 0.085% are NK cells that co-express PD1 and CD8, while 17.8% are CD8 T cells that express PD1 (Figure S7F). Since depletion of CD8 cells blocks the improved response to the treatment combination, the role of $PD1^+$ NK cells in the enhanced response to anti-PD1 upon doxorubicin is therefore likely limited. Together, our data confirm that CD8 T cells have a key role in driving the prolonged survival observed upon doxorubicin pre-treatment followed by anti-PD1 in PyMT BCBM.

We subsequently tested whether continuous administration of doxorubicin during anti-PD1 treatment would further improve survival outcomes compared with pre-treatment alone. Mice bearing PyMT BCBM lesions were pre-treated with vehicle or with doxorubicin prior to treatment with anti-PD1 alone or with anti-PD1 combined with doxorubicin (Figure S7D). Pre-treatment with doxorubicin followed by continuous treatment with doxorubicin had no advantage over pre-treatment with doxorubicin alone when combined with anti-PD1 (Figure S7E), demonstrating that pre-treatment with doxorubicin can improve anti-PD1 therapy without the need for long-term exposure to doxorubicin with increased toxicity.

Lastly, to test whether the combination treatment can be efficacious beyond the PyMT BCBM model, we generated a second BCBM model derived from mammary tumors from MMTV-Neu mice, which harbors an overexpression of Her2.[65] This model is clinically relevant considering that 31% of $Her2^+$ metastatic BC patients develop BCBM.[3] We established the Neu BCBM model using six rounds of enrichment in the brain and we generated organoids (from herein called "Neu BCBM organoids") from the last round of enrichment, similarly to the PyMT BCBM. Treating Neu BCBM organoids with low-dose doxorubicin stalled organoid growth but only moderately induced apoptosis by 3% (Figures 7A and 7B). Next, we made a cell line from the Neu BCBM organoids and we confirmed that doxorubicin treatment induces SA β-galactosidase activity *in vitro* (Figure 7C). Lastly, we intracranially injected Neu BCBM organoids and upon BCBM formation, mice were randomized into treatment groups with vehicle followed by IgG, doxorubicin followed by IgG, vehicle followed by anti-PD1, or doxorubicin followed by anti-PD1, as for the PyMT BCBM model (Figure 5). Mice were monitored until showing signs of sickness. Treatment with doxorubicin followed by IgG or with vehicle followed by anti-PD1 did

(D) Kaplan-Meier analyses of time to humane endpoint and mean survival from the beginning of the treatment and (E) mean survival for mice treated with pre-treatment with vehicle (saline) followed by IgG control (n = 5 mice); pre-treatment with vehicle (saline) followed by anti-PD1 antibody (n = 6 mice); pre-treatment with doxorubicin followed by IgG control (n = 6 mice); or pre-treatment with doxorubicin followed by anti-PD1 antibody (n = 8 mice).
See also Figure S7.

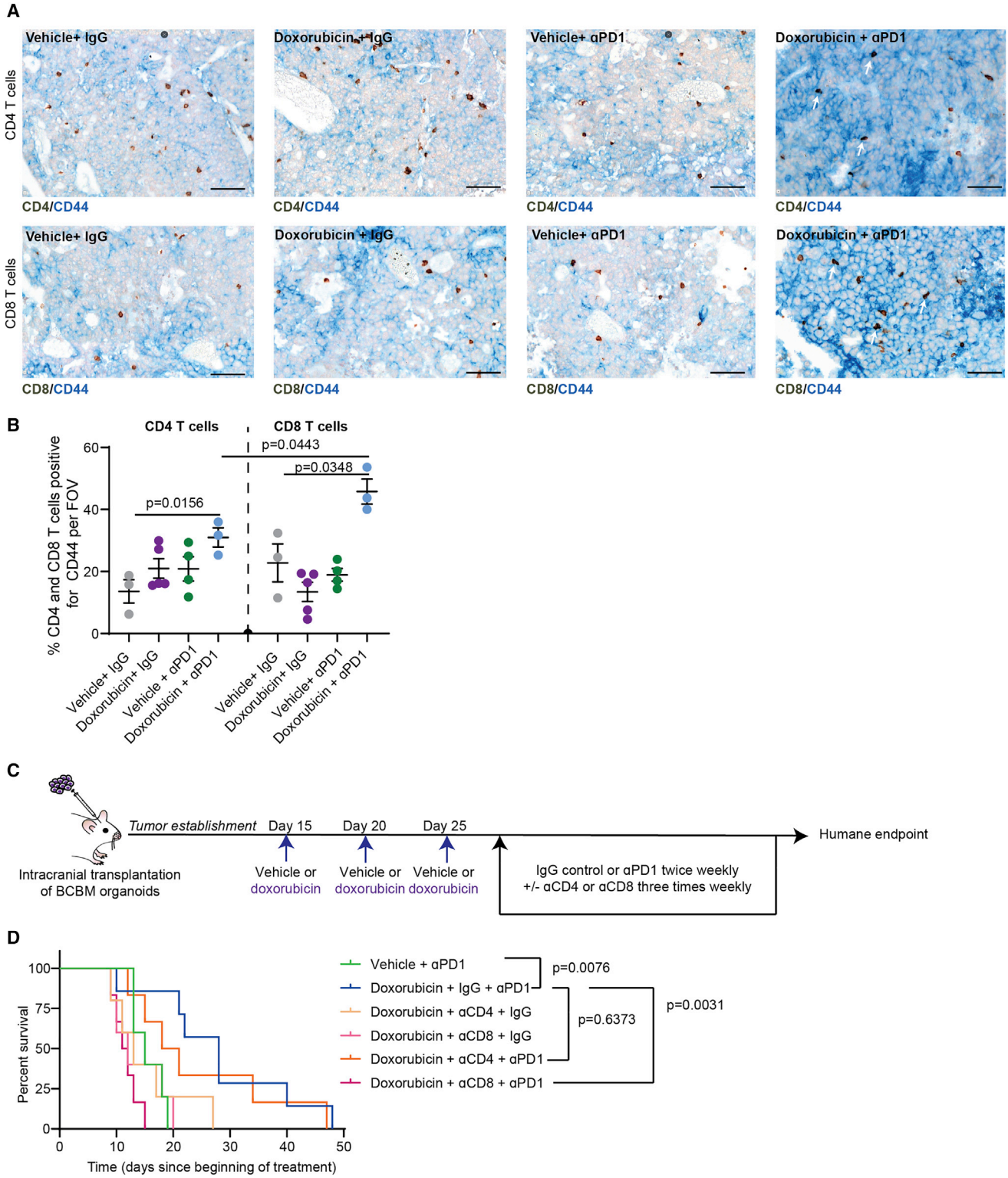

Figure 6. CD8 T cells drive the improved response to doxorubicin followed by anti-PD1

(A) Representative images of dual staining for CD4 and CD44 (top) and CD8 and CD44 (lower) in the PyMT BCBM upon treatment with vehicle (saline) followed by IgG control; pre-treatment with vehicle (saline) followed by anti-PD1 antibody; pre-treatment with doxorubicin followed by IgG control; or pre-treatment with doxorubicin followed by anti-PD1 antibody. White arrows point to double positive cells, scale bar, 100 μm.

(legend continued on next page)

not significantly alter mouse survival compared with vehicle followed by IgG (Figure 7D). However, similar to the PyMT BCBM, treatment with doxorubicin prior to anti-PD1 significantly improved mouse survival compared with monotherapies and with vehicle prior to IgG (Figure 7D). Together, this demonstrates the efficacy of pre-treatment with doxorubicin prior to anti-PD1 in a second model of BCBM, and warrants further consideration to introduce our combination therapy for BCBM patients.

DISCUSSION

Improving the outcomes of BCBM patients necessitates more systematic pre-clinical testing and optimization of therapeutic regimens. Immunotherapy has shown positive outcomes in solid cancer types including brain metastasis derived from melanoma or lung cancer but this remains limited for breast tumor.[6,66–68] Here, we used two pre-clinical immunocompetent mouse models of the disease to streamline immune-based treatments. Our PyMT BCBM model recapitulates key features of human BCBM with respect to intracranial growth, histopathological morphology, MRI profile, and immune landscape. Importantly, our mouse BCBM models can be used in the future to further design immune-based treatments in this disease and to explore mechanisms driving BCBM progression. As such, our combined treatment data demonstrate that inducing senescence via pre-treatment with doxorubicin triggers a recruitment of $PD1^+$ T cells to the BCBM, which subsequently can be used to improve the efficacy of anti-PD1 treatment. Specifically, we found that $CD8^+$ T cells are key drivers of the enhanced survival upon doxorubicin and anti-PD1. In addition, induction of senescence with doxorubicin did not correlate with important remodeling of the BTB, suggesting that other SASP factors are responsible for recruiting T cells to the BCBM.

Leveraging on the presence of senescent cells within a tumor mass to improve cancer treatment has previously been explored by us and others. For instance, inducing senescence has been shown to increase overall survival in lymphoma,[30] and can be combined with glucose blockade to specifically eliminate senescent cells.[69] Similarly in liver cancer, the induction of senescence combined with administration of senolytic agents can significantly reduce tumor growth.[70] In addition, the use of CAR T cells that specifically target senescent cancer cells has been shown to prolong survival in mice bearing lung adenocarcinoma.[71] Senescence can be induced in various ways, such as telomeric or genomic alterations, oncogene activation, epigenomic remodeling, or oxidative stress (reviewed in Faget et al.[27]). These various inducers of senescence will trigger the secretion of distinct SASP factors and this can partly explain the various and somewhat opposite effects of senescence in cancer. The influence of senescent cells on cancer progression remains, however, controversial, since previous studies have shown that SASP factors can both promote and halt cancer progression.[27,72] In addition, the role of cancer senescent cells in brain tumors remains under-studied. Here, we demonstrate that doxorubicin can be used to trigger senescence in BCBM, which in turn triggers a remodeling of the tumor immune landscape that can be used to improve immunotherapy in BCBM.

While we report an induction of senescence upon doxorubicin *in vivo*, we do not observe an effect of doxorubicin treatment on BCBM growth or mouse survival. Doxorubicin-induced senescence was previously shown to be accompanied by a mitogenic SASP,[73] therefore it is possible that senescent cells induce proliferation of their neighboring cells, which could explain the lack of effect of doxorubicin on tumor growth. In addition, considering that the recruited T cells upon doxorubicin express PD1, they may have reduced cytotoxic capacity and therefore not be capable of eradicating BCBM cells, which can explain the lack of efficacy of doxorubicin treatment alone.

In addition to the recruitment of T cells, we observed an increased number of NK cells expressing PD1 upon doxorubicin treatment, which has previously been linked to functional exhaustion of these cells.[74] NK cells can be recruited to clear senescent cells as a mechanism to maintain tissue integrity[75] and may therefore become exhausted when the number of senescent cells rise upon doxorubicin treatment. On the other hand, $PD1^+$ NK cells can also be cytotoxic[76]; however, we found that $CD8^+$ cells are critical drivers of the response to the combination treatment, and only a small percentage of $PD1^+$ NK cells recruited to the BCBM upon doxorubicin express CD8. Therefore, the contribution of NK cells to the improved survival upon doxorubicin followed by anti-PD1 appears limited.

Doxorubicin has been used to treat BC with extracranial diseases; however, it has failed to improve outcomes in BCBM. Attempts to improve the efficacy of doxorubicin in BCBM have been reported. For instance, engineering doxorubicin with liposomes to pass the BBB and the BTB is currently being assessed in the clinic (NCT01818713). Here, our data reveal that re-purposing the pro-senescence properties of doxorubicin can be used to successfully introduce immunotherapy with immune checkpoint blockade in BCBM. In addition, the improved efficacy of anti-PD1 following doxorubicin pre-treatment in our BCBM models is in line with findings from the TONIC trial in extracranial breast tumors,[51] and demonstrates that harnessing the immunomodulating, pro-senescence properties of

(B) Quantification of $CD44^+$ CD4 and $CD44^+$ CD8 T cells as a percentage of total CD4 or CD8 T cells, respectively, in the PyMT BCBM upon treatment with vehicle (saline) followed by IgG control (n = 3 mice), doxorubicin followed by IgG control (n = 5 mice), vehicle (saline) followed by anti-PD1 (n = 4 mice), or doxorubicin followed by anti-PD1 (n = 3 mice), at endpoint (relates to the mouse cohort depicted in Figures 5A–5C). Per tumor section, 4–5 fields of view were analyzed and averaged. Data are mean ± SEM.

(C) Schematic representation of experimental design and treatment timeline.

(D) Kaplan-Meier analyses of time to humane endpoint for mice treated with vehicle (saline) followed by anti-PD1 antibody (n = 5 mice); pre-treatment with doxorubicin followed by IgG control and anti-PD1 antibody (n = 6 mice); pre-treatment with doxorubicin followed by anti-CD4 or anti-CD8 antibody and IgG control (n = 5 mice); or pre-treatment with doxorubicin followed by anti-CD4 or anti-CD8 antibody and anti-PD1 antibody (n = 5 mice for CD4-depletion and n = 6 mice for CD8-depletion).

See also Figure S7.

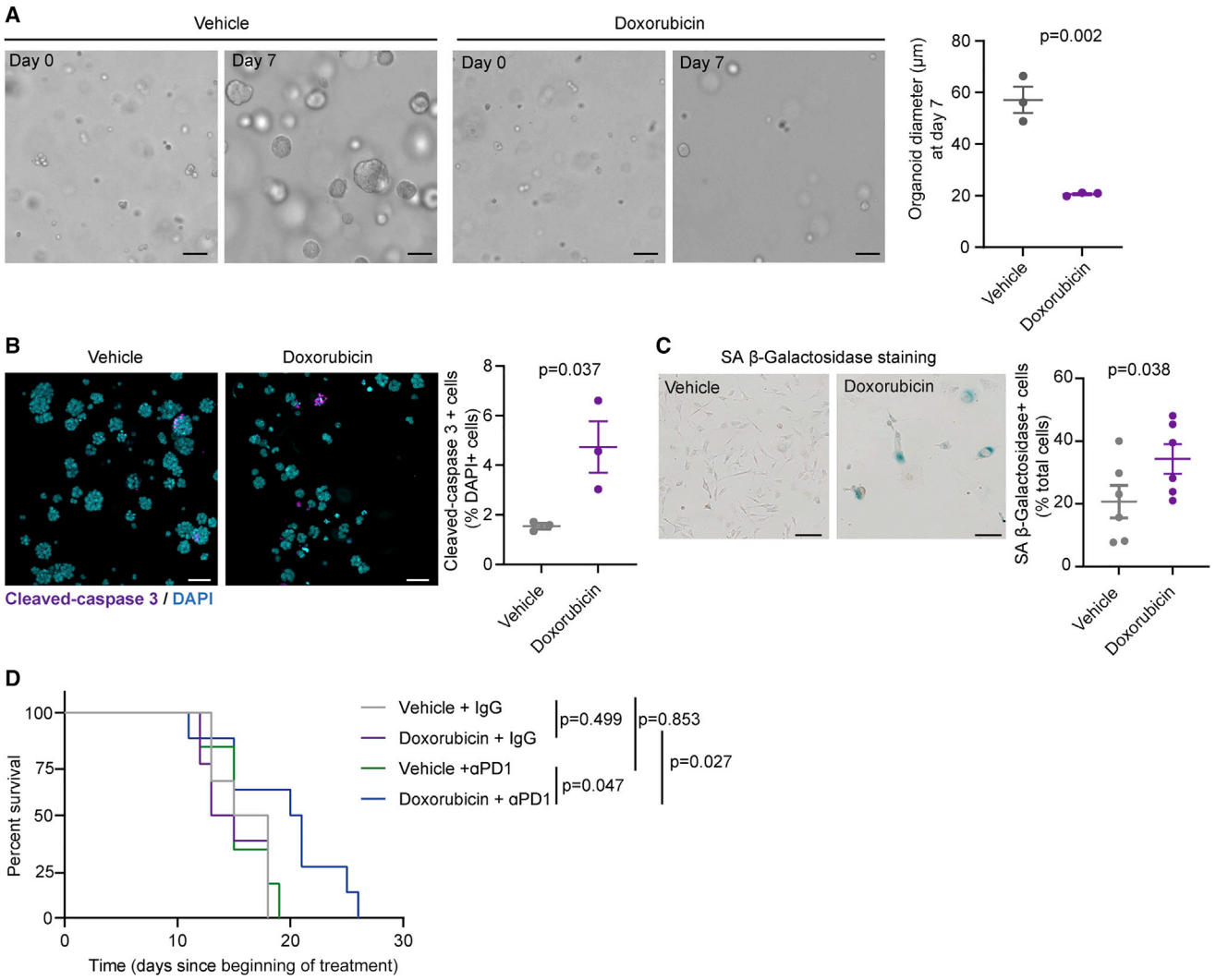

Figure 7. Doxorubicin induces senescence and improves the response to anti-PD1 in the Neu BCBM model

(A) Representative images of Neu BCBM organoids at day 0 and day 7 of treatment with vehicle (PBS) or with doxorubicin (20 nmol/L) and quantification of organoid diameter at day 7. n = 3 biological repeats. Scale bar, 50 μm.

(B) Representative images and quantification of cell apoptosis using immunofluorescence staining for cleaved-caspase 3 in Neu BCBM organoids after 7 days of treatment with vehicle (PBS) or doxorubicin (20 nmol/L), n = 3 biological repeats. Scale bar, 50 μm.

(C) Representative images of SA β-Galactosidase staining and quantification of the percentage of Neu BCBM cells positive for SA β-Galactosidase after 7 days of treatment with vehicle (PBS) or with doxorubicin (20 nmol/L), n = 6 biological repeats. Scale bar, 100 μm. p-values were determined using a paired nonparametric t test with a Mann-Whitney *U* correction.

(D) Kaplan-Meier analyses of time to humane endpoint for mice bearing Neu BCBM and from the beginning of the pre-treatment with vehicle (saline) followed by IgG control (n = 6 mice); pre-treatment with vehicle (saline) followed by anti-PD1 antibody (n = 6 mice); pre-treatment with doxorubicin followed by IgG control (n = 8 mice); or pre-treatment with doxorubicin followed by anti-PD1 antibody (n = 8 mice). Data are presented as mean ± SEM.

doxorubicin can be used to improve checkpoint inhibitor treatments in BCBM.

There are some limitations to our study. Firstly, our PyMT BCBM model does not spontaneously metastasize to the brain upon cardiac injection of the BCBM organoids. Indeed, no tumors were formed and we did not observe single tumor cells 6 months after intracardiac injection. Secondly, further research is needed to test whether BCBM can be sensitized to immune checkpoint inhibitors using other chemotherapies such as nab-paclitaxel and carboplatin/gemcitabine, which are currently being tested in combination with immunotherapy in BC patients with extracranial lesions.[15,51,77] In addition, radiotherapy, which is a standard-of-care for BCBM, can also induce senescence and may therefore also sensitize BCBM to immunotherapy.[78,79] Although our data suggest that doxorubicin pre-treatment could improve immunotherapy in BCBM, this strategy has yet to be used in the clinic. BCBM patients are not currently treated with doxorubicin, consequently validating our findings in the human

setting is not yet possible. Nevertheless, doxorubicin is already safely used in patients, and clinical trials would allow assessment of the efficacy of doxorubicin pre-treatment before anti-PD1 therapy for BCBM patients. In addition, it remains to be investigated whether first-line treatments for primary breast cancer or for patients with undetected BM, used in the clinic but not tested in our settings, have affected the ability of doxorubicin to recruit T cell to BCBMs and subsequently the efficiency of anti-PD1 treatment. Lastly, we used an anti-PD1 antibody that in addition to acting as an immune checkpoint inhibitor can also trigger depletion of specific $PD1^+$ T cell and NK cell subsets.[80] Further work is required to test the efficacy of Fc inactive anti-PD1 antibody upon treatment with doxorubicin.

In summary, our study provides evidence that inducing senescence using doxorubicin pre-treatment can sensitize BCBM to PD1 blockade. This opens avenues to introduce immune-based treatments for BCBM patients. Our data also provide insights into how chemotherapy-induced senescence can be used to improve immunotherapy, which may have important implications for strategies to combine induction of pro-senescence programs and immunotherapy in other cancer types.

Limitations of the study

There are some limitations to our study. Firstly, the metastatic capacity of our PyMT BCBM model is modest when the BCBM organoids are injected into the mouse carotid. In addition, the PyMT BCBM does not colonize the brain upon cardiac injection. This can in part be because we generated BCBM organoid lines rather than cell lines. While organoids faithfully mimic tumor heterogeneity and *in vivo* features of tumors, their ability to colonize the brain may be more modest than cell lines. However, the behavior of our BCBM organoids upon systemic injection is in line with a fairly periodic spread to the brain in BC patients. Therefore, our model cannot easily accommodate study of the early steps of metastatic spread to the brain, but can be readily used for preclinical studies in BCBM using intracranial injections. Secondly, the observed improvement in survival upon doxorubicin and anti-PD1 could be further validated by performing histopathological assessments of the BCBM at the same timepoint in the treatment; however, this cannot be performed in survival experiments. Lastly, although we observe induction of senescence in the BCBM upon doxorubicin, further work is needed to formally demonstrate that doxorubicin penetrates into the BCBM tissue.

STAR★METHODS

Detailed methods are provided in the online version of this paper and include the following:

SUPPLEMENTAL INFORMATION

Supplemental information can be found online at https://doi.org/10.1016/j.xcrm.2022.100821.

ACKNOWLEDGMENTS

The authors thank all members of the van Rheenen laboratory for critical reading of the manuscript. The authors also thank the Pathology Department, the Animal Research facility, the Flow Cytometry facility, and the Bioimaging facility of the Netherlands Cancer Institute and Pablo Lopez-Jimenez and Dr. van Duijnen (LUMC) for technical and scientific supports. This work was supported by the European Research Council Grant CANCER-RECURRENCE 648804, the CancerGenomics.nl (Netherlands Organisation for Scientific Research) program, the Josef Steiner Cancer Research Foundation, and the Dutch Cancer Society (grant 12049) (L.A.). A.S.M. is the recipient of a fellowship from the Portuguese Foundation for Science and Technology (FCT, GABBA program-PD/BD/105748/2014). C.V. is funded by a fellowship from the Human Frontier Science Program. D.A.P. was supported by the Dutch Cancer Society (KWF) grant UMCU-7141 awarded to P.L.J.d.K. K.H. received funding from the Swiss National Science Foundation. The funders had no role in the study design; in the collection, analysis, and interpretation of data; in the writing of the paper; or in the decision to submit the paper for publication.

AUTHOR CONTRIBUTIONS

Conceptualization: A.S.M., R.U.C., M.L.D.B., C.V., and J.v.R. Data curation, formal analysis and validation: A.S.M., C.V., L.C., S.V., R.U.C., D.A.P., M.v.G., C.C., L.t.B. Methodology and investigation: A.S.M., R.U.C., S.V., J.Y.S., K.H., P.L.J.d.K., L.t.B., G.B., L.A., O.v.T., C.V., J.v.R. Project administration and supervision: C.V. and J.v.R. Writing – original draft: A.S.M., R.U.C., C.V., and J.v.R. Writing – review and editing: J.Y.S., S.V., L.A., A.S.M., R.U.C., C.V., and J.v.R. Funding acquisition: A.S.M., C.V., J.v.R.

DECLARATION OF INTERESTS

P.L.J.d.K. is a co-founder and shareholder of Cleara Biotech BV, the Netherlands. D.A.P. works as a scientist at Cleara Biotech BV, the Netherlands.

CellPress
OPEN ACCESS

Received: November 12, 2021
Revised: September 2, 2022
Accepted: October 18, 2022
Published: November 15, 2022

REFERENCES

1. Lin, N.U., Bellon, J.R., and Winer, E.P. (2004). CNS metastases in breast cancer. J. Clin. Oncol. *22*, 3608–3617.
2. Bowman, K.M., and Kumthekar, P. (2018). Medical management of brain metastases and leptomeningeal disease in patients with breast carcinoma. Future Oncol. *14*, 391–407.
3. Kuksis, M., Gao, Y., Tran, W., Hoey, C., Kiss, A., Komorowski, A.S., Dhaliwal, A.J., Sahgal, A., Das, S., Chan, K.K., and Jerzak, K.J. (2021). The incidence of brain metastases among patients with metastatic breast cancer: a systematic review and meta-analysis. Neuro Oncol. *23*, 894–904.
4. Jacobson, A. (2022). Trastuzumab deruxtecan improves progression-free survival and intracranial response in patients with HER2-positive metastatic breast cancer and brain metastases. Oncol. *27*, S3–S4.
5. O'Sullivan, C.C., Davarpanah, N.N., Abraham, J., and Bates, S.E. (2017). Current challenges in the management of breast cancer brain metastases. Semin. Oncol. *44*, 85–100.
6. Goldberg, S.B., Gettinger, S.N., Mahajan, A., Chiang, A.C., Herbst, R.S., Sznol, M., Tsiouris, A.J., Cohen, J., Vortmeyer, A., Jilaveanu, L., et al. (2016). Pembrolizumab for patients with melanoma or non-small-cell lung cancer and untreated brain metastases: early analysis of a non-randomised, open-label, phase 2 trial. Lancet Oncol. *17*, 976–983.
7. Hodi, F.S., O'Day, S.J., McDermott, D.F., Weber, R.W., Sosman, J.A., Haanen, J.B., Gonzalez, R., Robert, C., Schadendorf, D., Hassel, J.C., et al. (2010). Improved survival with ipilimumab in patients with metastatic melanoma. N. Engl. J. Med. *363*, 711–723.
8. Marshall, H.T., and Djamgoz, M.B.A. (2018). Immuno-oncology: emerging targets and combination therapies. Front. Oncol. *8*, 315.
9. Waldman, A.D., Fritz, J.M., and Lenardo, M.J. (2020). A guide to cancer immunotherapy: from T cell basic science to clinical practice. Nat. Rev. Immunol. *20*, 651–668.
10. Couzin-Frankel, J. (2013). Breakthrough of the year 2013. Cancer immunotherapy. Science *342*, 1432–1433.
11. Engelhardt, B., Vajkoczy, P., and Weller, R.O. (2017). The movers and shapers in immune privilege of the CNS. Nat. Immunol. *18*, 123–131.
12. Louveau, A., Harris, T.H., and Kipnis, J. (2015). Revisiting the mechanisms of CNS immune privilege. Trends Immunol. *36*, 569–577.
13. Klemm, F., Maas, R.R., Bowman, R.L., Kornete, M., Soukup, K., Nassiri, S., Brouland, J.P., Iacobuzio-Donahue, C.A., Brennan, C., Tabar, V., et al. (2020). Interrogation of the microenvironmental landscape in brain tumors reveals disease-specific alterations of immune cells. Cell *181*, 1643–1660.e17.
14. Quail, D.F., and Joyce, J.A. (2017). The microenvironmental landscape of brain tumors. Cancer Cell *31*, 326–341.
15. Schmid, P., Adams, S., Rugo, H.S., Schneeweiss, A., Barrios, C.H., Iwata, H., Diéras, V., Hegg, R., Im, S.A., Shaw Wright, G., et al. (2018). Atezolizumab and nab-paclitaxel in advanced triple-negative breast cancer. N. Engl. J. Med. *379*, 2108–2121.
16. Murthy, R.K., Loi, S., Okines, A., Paplomata, E., Hamilton, E., Hurvitz, S.A., Lin, N.U., Borges, V., Abramson, V., Anders, C., et al. (2020). Tucatinib, trastuzumab, and capecitabine for HER2-positive metastatic breast cancer. N. Engl. J. Med. *382*, 597–609.
17. Tolaney, S.M., Sahebjam, S., Le Rhun, E., Bachelot, T., Kabos, P., Awada, A., Yardley, D., Chan, A., Conte, P., Diéras, V., et al. (2020). A phase II study of abemaciclib in patients with brain metastases secondary to hormone receptor-positive breast cancer. Clin. Cancer Res. *26*, 5310–5319.
18. Galluzzi, L., Humeau, J., Buqué, A., Zitvogel, L., and Kroemer, G. (2020). Immunostimulation with chemotherapy in the era of immune checkpoint inhibitors. Nat. Rev. Clin. Oncol. *17*, 725–741.
19. Kersten, K., Salvagno, C., and de Visser, K.E. (2015). Exploiting the immunomodulatory properties of chemotherapeutic drugs to improve the success of cancer immunotherapy. Front. Immunol. *6*, 516.
20. Olson, O.C., Kim, H., Quail, D.F., Foley, E.A., and Joyce, J.A. (2017). Tumor-associated macrophages suppress the cytotoxic activity of antimitotic agents. Cell Rep. *19*, 101–113.
21. Zingoni, A., Fionda, C., Borrelli, C., Cippitelli, M., Santoni, A., and Soriani, A. (2017). Natural killer cell response to chemotherapy-stressed cancer cells: role in tumor immunosurveillance. Front. Immunol. *8*, 1194.
22. Ruffell, B., Chang-Strachan, D., Chan, V., Rosenbusch, A., Ho, C.M.T., Pryer, N., Daniel, D., Hwang, E.S., Rugo, H.S., and Coussens, L.M. (2014). Macrophage IL-10 blocks CD8+ T cell-dependent responses to chemotherapy by suppressing IL-12 expression in intratumoral dendritic cells. Cancer Cell *26*, 623–637.
23. Junankar, S., Shay, G., Jurczyluk, J., Ali, N., Down, J., Pocock, N., Parker, A., Nguyen, A., Sun, S., Kashemirov, B., et al. (2015). Real-time intravital imaging establishes tumor-associated macrophages as the extraskeletal target of bisphosphonate action in cancer. Cancer Discov. *5*, 35–42.
24. Page, D.B., Beal, K., Linch, S.N., Spinelli, K.J., Rodine, M., Halpenny, D., Modi, S., Patil, S., Young, R.J., Kaley, T., et al. (2022). Brain radiotherapy, tremelimumab-mediated CTLA-4-directed blockade +/- trastuzumab in patients with breast cancer brain metastases. NPJ Breast Cancer *8*, 50.
25. Sevenich, L. (2019). Turning "Cold" into "Hot" Tumors-opportunities and challenges for radio-immunotherapy against primary and metastatic brain cancers. Front. Oncol. *9*, 163.
26. Kumthekar, P., Tang, S.C., Brenner, A.J., Kesari, S., Piccioni, D.E., Anders, C., Carrillo, J., Chalasani, P., Kabos, P., Puhalla, S., et al. (2020). ANG1005, a brain-penetrating peptide-drug conjugate, shows activity in patients with breast cancer with leptomeningeal carcinomatosis and recurrent brain metastases. Clin. Cancer Res. *26*, 2789–2799.
27. Faget, D.V., Ren, Q., and Stewart, S.A. (2019). Unmasking senescence: context-dependent effects of SASP in cancer. Nat. Rev. Cancer *19*, 439–453.
28. Ruscetti, M., Morris, J.P., 4th, Mezzadra, R., Russell, J., Leibold, J., Romesser, P.B., Simon, J., Kulick, A., Ho, Y.J., Fennell, M., et al. (2020). Senescence-induced vascular remodeling creates therapeutic vulnerabilities in pancreas cancer. Cell *181*, 424–441.e21.
29. Ewald, J.A., Desotelle, J.A., Wilding, G., and Jarrard, D.F. (2010). Therapy-induced senescence in cancer. J. Natl. Cancer Inst. *102*, 1536–1546.
30. Schmitt, C.A., Fridman, J.S., Yang, M., Lee, S., Baranov, E., Hoffman, R.M., and Lowe, S.W. (2002). A senescence program controlled by p53 and p16INK4a contributes to the outcome of cancer therapy. Cell *109*, 335–346.
31. Ruscetti, M., Leibold, J., Bott, M.J., Fennell, M., Kulick, A., Salgado, N.R., Chen, C.C., Ho, Y.J., Sanchez-Rivera, F.J., Feucht, J., et al. (2018). NK cell-mediated cytotoxicity contributes to tumor control by a cytostatic drug combination. Science *362*, 1416–1422.
32. Su, D., Zhu, S., Han, X., Feng, Y., Huang, H., Ren, G., Pan, L., Zhang, Y., Lu, J., and Huang, B. (2009). BMP4-Smad signaling pathway mediates adriamycin-induced premature senescence in lung cancer cells. J. Biol. Chem. *284*, 12153–12164.
33. Chastagner, P., Sudour, H., Mriouah, J., Barberi-Heyob, M., Bernier-Chastagner, V., and Pinel, S. (2015). Preclinical studies of pegylated- and non-pegylated liposomal forms of doxorubicin as radiosensitizer on orthotopic high-grade glioma xenografts. Pharm. Res. (N. Y.) *32*, 158–166.
34. Liu, Y., Yang, Y., Liu, X., and Jiang, T. (2008). Quantification of pegylated liposomal doxorubicin and doxorubicinol in rat plasma by liquid chromatography/electrospray tandem mass spectroscopy: application to preclinical pharmacokinetic studies. Talanta *74*, 887–895.

35. Vail, D.M., Amantea, M.A., Colbern, G.T., Martin, F.J., Hilger, R.A., and Working, P.K. (2004). Pegylated liposomal doxorubicin: proof of principle using preclinical animal models and pharmacokinetic studies. Semin. Oncol. *31*, 16–35.

36. Beerling, E., Seinstra, D., de Wit, E., Kester, L., van der Velden, D., Maynard, C., Schäfer, R., van Diest, P., Voest, E., van Oudenaarden, A., et al. (2016). Plasticity between epithelial and mesenchymal states unlinks EMT from metastasis-enhancing stem cell capacity. Cell Rep. *14*, 2281–2288.

37. Margarido, A.S., Uceda-Castro, R., Hahn, K., de Bruijn, R., Kester, L., Hofland, I., Lohuis, J., Seinstra, D., Broeks, A., Jonkers, J., et al. (2022). Epithelial-to-Mesenchymal transition drives invasiveness of breast cancer brain metastases. Cancers *14*, 3115.

38. Debnath, J., and Brugge, J.S. (2005). Modelling glandular epithelial cancers in three-dimensional cultures. Nat. Rev. Cancer *5*, 675–688.

39. Drost, J., and Clevers, H. (2018). Organoids in cancer research. Nat. Rev. Cancer *18*, 407–418.

40. Weaver, V.M., Lelièvre, S., Lakins, J.N., Chrenek, M.A., Jones, J.C.R., Giancotti, F., Werb, Z., and Bissell, M.J. (2002). beta4 integrin-dependent formation of polarized three-dimensional architecture confers resistance to apoptosis in normal and malignant mammary epithelium. Cancer Cell *2*, 205–216.

41. Rippaus, N., Taggart, D., Williams, J., Andreou, T., Wurdak, H., Wronski, K., and Lorger, M. (2016). Metastatic site-specific polarization of macrophages in intracranial breast cancer metastases. Oncotarget *7*, 41473–41487.

42. Howe, F.A., Barton, S.J., Cudlip, S.A., Stubbs, M., Saunders, D.E., Murphy, M., Wilkins, P., Opstad, K.S., Doyle, V.L., McLean, M.A., et al. (2003). Metabolic profiles of human brain tumors using quantitative in vivo 1H magnetic resonance spectroscopy. Magn. Reson. Med. *49*, 223–232.

43. Miller, B.L. (1991). A review of chemical issues in 1H NMR spectroscopy: N-acetyl-L-aspartate, creatine and choline. NMR Biomed. *4*, 47–52.

44. Topalian, S.L., Taube, J.M., Anders, R.A., and Pardoll, D.M. (2016). Mechanism-driven biomarkers to guide immune checkpoint blockade in cancer therapy. Nat. Rev. Cancer *16*, 275–287.

45. Iwamoto, T., Niikura, N., Ogiya, R., Yasojima, H., Watanabe, K.I., Kanbayashi, C., Tsuneizumi, M., Matsui, A., Fujisawa, T., Iwasa, T., et al. (2019). Distinct gene expression profiles between primary breast cancers and brain metastases from pair-matched samples. Sci. Rep. *9*, 13343.

46. Duchnowska, R., Pęksa, R., Radecka, B., Mandat, T., Trojanowski, T., Jarosz, B., Czartoryska-Arłukowicz, B., Olszewski, W.P., Och, W., Kalinka-Warzocha, E., et al. (2016). Immune response in breast cancer brain metastasis and their microenvironment: the role of the PD-1/PD-L axis. Breast Cancer Res. *18*, 43.

47. Baar, M.P., Brandt, R.M.C., Putavet, D.A., Klein, J.D.D., Derks, K.W.J., Bourgeois, B.R.M., Stryeck, S., Rijksen, Y., van Willigenburg, H., Feijtel, D.A., et al. (2017). Targeted apoptosis of senescent cells restores tissue homeostasis in response to chemotoxicity and aging. Cell *169*, 132–147.e16.

48. Wang, A.S., Ong, P.F., Chojnowski, A., Clavel, C., and Dreesen, O. (2017). Loss of lamin B1 is a biomarker to quantify cellular senescence in photoaged skin. Sci. Rep. *7*, 15678.

49. Coffinier, C., Jung, H.J., Nobumori, C., Chang, S., Tu, Y., Barnes, R.H., 2nd, Yoshinaga, Y., de Jong, P.J., Vergnes, L., Reue, K., et al. (2011). Deficiencies in lamin B1 and lamin B2 cause neurodevelopmental defects and distinct nuclear shape abnormalities in neurons. Mol. Biol. Cell *22*, 4683–4693.

50. Freund, A., Laberge, R.M., Demaria, M., and Campisi, J. (2012). Lamin B1 loss is a senescence-associated biomarker. Mol. Biol. Cell *23*, 2066–2075.

51. Voorwerk, L., Slagter, M., Horlings, H.M., Sikorska, K., van de Vijver, K.K., de Maaker, M., Nederlof, I., Kluin, R.J.C., Warren, S., Ong, S., et al. (2019). Immune induction strategies in metastatic triple-negative breast cancer to enhance the sensitivity to PD-1 blockade: the TONIC trial. Nat. Med. *25*, 920–928.

52. Toso, A., Revandkar, A., Di Mitri, D., Guccini, I., Proietti, M., Sarti, M., Pinton, S., Zhang, J., Kalathur, M., Civenni, G., et al. (2014). Enhancing chemotherapy efficacy in Pten-deficient prostate tumors by activating the senescence-associated antitumor immunity. Cell Rep. *9*, 75–89.

53. Dou, Z., Ghosh, K., Vizioli, M.G., Zhu, J., Sen, P., Wangensteen, K.J., Simithy, J., Lan, Y., Lin, Y., Zhou, Z., et al. (2017). Cytoplasmic chromatin triggers inflammation in senescence and cancer. Nature *550*, 402–406.

54. Glück, S., Guey, B., Gulen, M.F., Wolter, K., Kang, T.W., Schmacke, N.A., Bridgeman, A., Rehwinkel, J., Zender, L., and Ablasser, A. (2017). Innate immune sensing of cytosolic chromatin fragments through cGAS promotes senescence. Nat. Cell Biol. *19*, 1061–1070.

55. Kang, T.W., Yevsa, T., Woller, N., Hoenicke, L., Wuestefeld, T., Dauch, D., Hohmeyer, A., Gereke, M., Rudalska, R., Potapova, A., et al. (2011). Senescence surveillance of pre-malignant hepatocytes limits liver cancer development. Nature *479*, 547–551.

56. Ritsma, L., Vrisekoop, N., and van Rheenen, J. (2013). *In vivo* imaging and histochemistry are combined in the cryosection labelling and intravital microscopy technique. Nat. Commun. *4*, 2366. https://doi.org/10.1038/ncomms3366.

57. Lagares, D., Santos, A., Grasberger, P.E., Liu, F., Probst, C.K., Rahimi, R.A., Sakai, N., Kuehl, T., Ryan, J., Bhola, P., et al. (2017). Targeted apoptosis of myofibroblasts with the BH3 mimetic ABT-263 reverses established fibrosis. Sci. Transl. Med. *9*, eaal3765.

58. Chang, J., Wang, Y., Shao, L., Laberge, R.M., Demaria, M., Campisi, J., Janakiraman, K., Sharpless, N.E., Ding, S., Feng, W., et al. (2016). Clearance of senescent cells by ABT263 rejuvenates aged hematopoietic stem cells in mice. Nat. Med. *22*, 78–83.

59. Yu, X., Dobrikov, M., Keir, S.T., Gromeier, M., Pastan, I.H., Reisfeld, R., Bigner, D.D., and Chandramohan, V. (2019). Synergistic antitumor effects of 9.2.27-PE38KDEL and ABT-737 in primary and metastatic brain tumors. PLoS One *14*, e0210608.

60. Tarantini, S., Balasubramanian, P., Delfavero, J., Csipo, T., Yabluchanskiy, A., Kiss, T., Nyúl-Tóth, Á., Mukli, P., Toth, P., Ahire, C., et al. (2021). Treatment with the BCL-2/BCL-xL inhibitor senolytic drug ABT263/Navitoclax improves functional hyperemia in aged mice. Geroscience *43*, 2427–2440.

61. Lim, S., Kim, T.J., Kim, Y.J., Kim, C., Ko, S.B., and Kim, B.S. (2021). Senolytic therapy for cerebral ischemia-reperfusion injury. Int. J. Mol. Sci. *22*, 11967.

62. Hunt, B.J., and Jurd, K.M. (1998). Endothelial cell activation. A central pathophysiological process. BMJ *316*, 1328–1329.

63. Huet, S., Groux, H., Caillou, B., Valentin, H., Prieur, A.M., and Bernard, A. (1989). CD44 contributes to T cell activation. J. Immunol. *143*, 798–801.

64. McKinney, E.F., Cuthbertson, I., Harris, K.M., Smilek, D.E., Connor, C., Manferrari, G., Carr, E.J., Zamvil, S.S., and Smith, K.G.C. (2021). A CD8(+) NK cell transcriptomic signature associated with clinical outcome in relapsing remitting multiple sclerosis. Nat. Commun. *12*, 635.

65. Boggio, K., Nicoletti, G., Di Carlo, E., Cavallo, F., Landuzzi, L., Melani, C., Giovarelli, M., Rossi, I., Nanni, P., De Giovanni, C., et al. (1998). Interleukin 12-mediated prevention of spontaneous mammary adenocarcinomas in two lines of Her-2/neu transgenic mice. J. Exp. Med. *188*, 589–596.

66. Vilariño, N., Bruna, J., Bosch-Barrera, J., Valiente, M., and Nadal, E. (2020). Immunotherapy in NSCLC patients with brain metastases. Understanding brain tumor microenvironment and dissecting outcomes from immune checkpoint blockade in the clinic. Cancer Treat Rev. *89*, 102067.

67. Tawbi, H.A., Forsyth, P.A., Algazi, A., Hamid, O., Hodi, F.S., Moschos, S.J., Khushalani, N.I., Lewis, K., Lao, C.D., Postow, M.A., et al. (2018). Combined nivolumab and ipilimumab in melanoma metastatic to the brain. N. Engl. J. Med. *379*, 722–730.

68. Cloughesy, T.F., Mochizuki, A.Y., Orpilla, J.R., Hugo, W., Lee, A.H., Davidson, T.B., Wang, A.C., Ellingson, B.M., Rytlewski, J.A., Sanders, C.M.,

et al. (2019). Neoadjuvant anti-PD-1 immunotherapy promotes a survival benefit with intratumoral and systemic immune responses in recurrent glioblastoma. Nat. Med. *25*, 477–486.

69. Dörr, J.R., Yu, Y., Milanovic, M., Beuster, G., Zasada, C., Däbritz, J.H.M., Lisec, J., Lenze, D., Gerhardt, A., Schleicher, K., et al. (2013). Synthetic lethal metabolic targeting of cellular senescence in cancer therapy. Nature *501*, 421–425.
70. Wang, C., Vegna, S., Jin, H., Benedict, B., Lieftink, C., Ramirez, C., de Oliveira, R.L., Morris, B., Gadiot, J., Wang, W., et al. (2019). Inducing and exploiting vulnerabilities for the treatment of liver cancer. Nature *574*, 268–272.
71. Amor, C., Feucht, J., Leibold, J., Ho, Y.J., Zhu, C., Alonso-Curbelo, D., Mansilla-Soto, J., Boyer, J.A., Li, X., Giavridis, T., et al. (2020). Senolytic CAR T cells reverse senescence-associated pathologies. Nature *583*, 127–132.
72. Wang, B., Kohli, J., and Demaria, M. (2020). Senescent cells in cancer therapy: friends or foes? Trends Cancer *6*, 838–857.
73. Jackson, J.G., Pant, V., Li, Q., Chang, L.L., Quintás-Cardama, A., Garza, D., Tavana, O., Yang, P., Manshouri, T., Li, Y., et al. (2012). p53-mediated senescence impairs the apoptotic response to chemotherapy and clinical outcome in breast cancer. Cancer Cell *21*, 793–806.
74. Beldi-Ferchiou, A., Lambert, M., Dogniaux, S., Vély, F., Vivier, E., Olive, D., Dupuy, S., Levasseur, F., Zucman, D., Lebbé, C., et al. (2016). PD-1 mediates functional exhaustion of activated NK cells in patients with Kaposi sarcoma. Oncotarget *7*, 72961–72977.
75. Pesce, S., Greppi, M., Grossi, F., Del Zotto, G., Moretta, L., Sivori, S., Genova, C., and Marcenaro, E. (2019). PD/1-PD-Ls checkpoint: insight on the potential role of NK cells. Front. Immunol. *10*, 1242.
76. Hsu, J., Hodgins, J.J., Marathe, M., Nicolai, C.J., Bourgeois-Daigneault, M.C., Trevino, T.N., Azimi, C.S., Scheer, A.K., Randolph, H.E., Thompson, T.W., et al. (2018). Contribution of NK cells to immunotherapy mediated by PD-1/PD-L1 blockade. J. Clin. Invest. *128*, 4654–4668.
77. Cortes, J., Cescon, D.W., Rugo, H.S., Nowecki, Z., Im, S.-A., Yusof, M.M., Gallardo, C., Lipatov, O., Barrios, C.H., Holgado, E., et al. (2020). KEYNOTE-355: randomized, double-blind, phase III study of pembrolizumab + chemotherapy versus placebo + chemotherapy for previously untreated locally recurrent inoperable or metastatic triple-negative breast cancer. J. Clin. Oncol. *38*, 1000.
78. Tabasso, A.F.S., Jones, D.J.L., Jones, G.D.D., and Macip, S. (2019). Radiotherapy-induced senescence and its effects on responses to treatment. Clin. Oncol. *31*, 283–289.
79. Putavet, D.A., and de Keizer, P.L.J. (2021). Residual disease in glioma recurrence: a dangerous liaison with senescence. Cancers *13*, 1560.
80. Dahan, R., Sega, E., Engelhardt, J., Selby, M., Korman, A.J., and Ravetch, J.V. (2015). FcgammaRs modulate the anti-tumor activity of antibodies targeting the PD-1/PD-L1 Axis. Cancer Cell *28*, 285–295.
81. Lignelli, A., and Khandji, A.G. (2011). Review of imaging techniques in the diagnosis and management of brain metastases. Neurosurg. Clin. *22*, 15–25.
82. Hourani, R., Brant, L.J., Rizk, T., Weingart, J.D., Barker, P.B., and Horská, A. (2008). Can proton MR spectroscopic and perfusion imaging differentiate between neoplastic and nonneoplastic brain lesions in adults? AJNR. Am. J. Neuroradiol. *29*, 366–372.
83. Zhang, C., Lowery, F.J., and Yu, D. (2017). Intracarotid cancer cell injection to produce mouse models of brain metastasis. JoVE *120*.

STAR★METHODS

KEY RESOURCES TABLE

REAGENT or RESOURCE	SOURCE	IDENTIFIER
Antibodies		
Anti-mouse Cleaved-Caspase 3 (Asp175)	Cell Signaling Technology	9661; RRID:AB_2341188
Chicken anti-Rabbit Alexa Fluor 647	Thermo Fisher Scientific	9661; RRID:AB_2341188
Anti-mouse E-Cadherin	Cell Signaling Technology	3195; RRID:AB_2291471
Anti-mouse Keratin 8	DSHB University of Iowa, Troma 1	RRID: AB_531826
Anti-mouse GFAP	BioTrend	BT46-5002-04
Anti-mouse Pankeratin	Thermo Fisher Scientific	MS-343-P; RRID: MS-343-P
Anti-mouse CD4	eBiosciences	14_9766_80; RRID:AB_2573007
Anti-mouse CD8	eBiosciences	14-0808; RRID: AB_2572860
Anti-mouse PD1	Cell Signaling Technology	84651; RRID: AB_2800041
Anti-mouse Ly6G	BD Biosciences	551459; RRID:AB_394206
Anti-mouse FoxP3	eBiosciences	14-5773-82; RRID:AB_467576
Anti-mouse F4/80	Cell Signaling Technology	70076; RRID:AB_2799771
Anti-mouse CD44 (HCAM)	Santa Cruz	sc-18849; RRID:AB_2074688
Goat-α-Rat-Biotynated secondary antibody	SouthernBiotech	3052-08; RRID:AB_2795846
Anti-human CD4	Cell Marque	EP204
Anti-human CD8	Dako Omnis	GA263
Anti-human PD-L1	Dako Omnis	GE006
Anti-human GFAP	Dako Omnis	Z0334
Anti-human E-Cadherin	Dako Omnis	GA059
Anti-human pankeratin	Dako Omnis	IR053
Anti-human keratin 18	Dako Omnis	N/A
anti-mouse CD4-eFluor660	eBioscience	50-0041-82; RRID:AB_10609337
anti-mouse CD8-eFluor660	eBioscience	50-0081-82; RRID:AB_10596646
anti-mouse CD31	BD Biosciences	550274; RRID:AB_393571
anti-mouse VCAM-1/CD106	R&D Systems	AF643-SP
anti-mouse ICAM/CD54	R&D Systems	AF796-SP
anti-mouse NG2 Chondroitin Sulfate Proteoglycan	Millipore	AB5320; RRID:AB_91789
anti-mouse α-smooth muscle actin	Sigma-Aldrich	A5228; RRID:AB_262054
Anti-mouse CD3 BV421	BD Bioscience	564008; RRID:AB_2732058
anti-mouse Ki67 Alexa Fluor 647	BD Pharmigen	558615; RRID:AB_647130
anti-CD11b BV650	Biolegend	101259; RRID:AB_2566568
Anti-mouse CD45 Alexa Fluor 700	Biolegend	103123; RRID:AB_493534
Anti-mouse CD4 APC	Biolegend	100412; RRID:AB_312697
Anti-mouse CD8 FITC	eBioscience	11-0081-82; RRID:AB_464915
Anti-mouse NK1.1	Biolegend	108713; RRID:AB_389363
Anti-mouse Ki67 BV786	BD Bioscience	558615; RRID:AB_647130
Anti-mouse PD-1 BV421	BD Bioscience	562584; RRID:AB_2737668
Anti-mouse CD69 PE-DAZZLE	Biolegend	104535; RRID:AB_2565582
Anti-mouse FoxP3 PE-Cy5.5	Biolegend	35-5773-82; RRID:AB_11218094
Anti-mouse Ly6G APC	Biolegend	127613; RRID:AB_1877163
Anti-mouse Ly6C BV605	Biolegend	128035; RRID:AB_2562352
Anti-Mouse CD49d PE-Cy7	Biolegend	103705; RRID:AB_313046
Anti-mouse Granzyme B Pacific Blue	Biolegend	515407; RRID:AB_2562195
Lamin B1	Abcam, clone GR3244890-2	ab16048

(*Continued on next page*)

Continued

REAGENT or RESOURCE	SOURCE	IDENTIFIER
Biological samples		
Human BCBM paraffin blocks	Leiden University Medical Center	N/A
Chemicals, peptides, and recombinant proteins		
Advanced Dulbecco's Modified Eagle Medium (DMEM) F/12 Glutamax	Thermo Fisher Scientific	10565018
Roswell Park Memorial Institute (RPMI) 1640	Thermo Fisher Scientific	21875034
B27	Thermo Fisher Scientific	17504001
Fetal Bovine Serum (FBS)	Thermo Fisher Scientific	A4766801
EGF	Thermo Fisher Scientific	53003018
Insulin	Sigma Aldrich	I0516
Cultrex PathClear Reduced Growth Factor Basement Membrane Extract Type 2	R&D Systems	3533-005-02
TrypLE	Thermo Fisher Scientific	12605-010
Freezing medium	Thermo Fisher Scientific	12648-010
Collagenase A	Roche	10103586001
Hepes	Thermo Fisher Scientific	15630106
Streptomycin/penicillin	Thermo Fisher Scientific	15140122
DNAse I	Roche	10104159001
DAPI	Thermo Fisher Scientific	D1306
Opti-MEM	Thermo Fisher Scientific	31985070
Polybrene	Sigma Aldrich	TR-1003-G
Y-27632	Bio Connect	S1049
FGF	Thermo Fisher Scientific	PHG0261
Puromycin	Thermo Fisher Scientific	A1113803
Lipofectamine 2000	Thermo Fisher Scientific	11668019
Rimadyl (carprofen)	Zoetis	N/A
Temgesic (buprenorphine)	Indivior Europe Limited	N/A
Duratears	Alcon	N/A
Lidocaine	Fresenius Kabi	N/A
Bupivacaine	Actavis, Aurobindo Pharma B.V.	N/A
Doxorubicin	Actavis	N/A
ABT263	MedKoo	201970
*InVivo*MAb rat IgG2b isotype control, clone LTF-2	BioXCell	BE0090
*InVivo*MAb rat IgG2b isotype control, clone 2A3	BioXCell	BE0089
*InVivo*MAb anti-mouse CD4, clone GK1.5	BioXCell	BE003-1
*InVivo*MAb anti-mouse CD8, clone YTS 169.4	BioXCell	BP0117
*InVivo*MAb anti-mouse PD1, clone RMP1-14	BioXCell	BE0146
Fc block CD16/CD32, clone 2.4G2	BD Biosciences	553141
Permeabilization kit	Thermo Fisher Scientific	00-5523-00
Beetle Luciferin	Promega	E1605
Gadoterate meglumine (Dotarem®)	Guerbet, Villepinte, France	N/A
OCT Tissue Tek	Thermo Fisher Scientific	11381785
Hoechst 33342	Thermo Fisher Scientific	H3570
ProLong Glass Antifade Mountant	Thermo Fisher Scientific	P3680
7-AAD dye	Biolegend	420404
Power SYBR Green PCR Master Mix	Thermo Fischer Scientific	A25777
IL2	Thermo Fischer Scientific	PMC0025
Ultraglutamine	Lonza	BE17-605E/U1
PMA	Sigma Aldrich	
Ionomycin	Sigma Aldrich	

(*Continued on next page*)

Continued

REAGENT or RESOURCE	SOURCE	IDENTIFIER
Vectashield hard set	Vectorlab	H-1400-10
Foxp3 fixation/permeabilization buffer	eBioscience	00-5523-00
HRP visualization in NovaRed	Vector Laboratories	SK-4800
AP visualization in blue	Vector Laboratories	SK-5300
Trizol	Invitrogen Life Technology	15596018
Critical commercial assays		
MycoAlert PLUS Kit	Lonza	LT07-118
Brain Tumor Dissociation kit	Miltenyi Biotec	130-095-942
SA β-galactosidase staining kit (staining of tissues)	Sigma Aldrich	11828673001
Senescence Cells Histochemical Staining Kit (*in vitro* staining)	Sigma-Aldrich	CS0030
High Capacity cDNA Reverse Transcription kit	ThermoFischer Scientific	4368814
Experimental models: Cell lines		
Mouse BCBM organoids and cells	Generated for this manuscript, available upon request to the lead contact.	N/A
Experimental models: Organisms/strains		
Mus musculus FVB/NRj	Janvier Labs	N/A
Mus musculus FVB/MMTV-PyMT-e-Cadherin-CFP	Beerling et al.[36]	N/A
Mus musculus FVB/N-Tg(MMTVNeu)202Mul/J	The Jackson laboratory	002376
Oligonucleotides		
FOXO4: forward: TCTACGAATGGATGGTCCGCAC, reverse: CTTGCTGTGCAAGGACAGGTTG	Integrated DNA Technologies |IDT	N/A
CDKN2A: forward: TGTTGAGGCTAGAGAGGATCTTG, reverse: CGAATCTGCACCGTAGTTGAGC	Integrated DNA Technologies |IDT	N/A
Ki67: forward: CTGCCTGCGAAGAGAGCATC, reverse: AGCTCCACTTCGCCTTTTGG	Integrated DNA Technologies |IDT	N/A
GAPDH: forward: GGGTTCCTATAAATACGGACTGC, reverse: CCATTTTGTCTACGGGACGA	Integrated DNA Technologies |IDT	N/A
Recombinant DNA		
UBC-Firefly-Luciferase	Generated for this manuscript, available upon request to the lead contact	N/A
UBC-H2B-Dendra2-puromycin	Generated for this manuscript, available upon request to the lead contact	N/A
psPAX2	Addgene	12260
PMD2.G	Addgene	12259
Software and algorithms		
AxioVision 4 software	Carl Zeiss Vision, München, Germany	N/A
FlowJo software 10.6.1	BD Biosciences	https://www.flowjo.com/
Paravision software, v6.0.1	Bruker	N/A
Fiji	https://imagej.net	2.1.0/1.53h
Huygens	Scientific Volume Imaging	https://svi.nl/Huygens-Software
ZEN	Zeiss	2.6 (Blue edition)
Prism	GraphPad	9.0.0 (86)
Imaris	Oxford Instruments	9.3.1
Other		
7 Tesla BioSpec 70/20 USR	Bruker; Billerica, MA USA	N/A
IVIS200 camera	PerkinElmer; Waltham, MA USA	N/A
24-well plate	Greiner bio-one	662160
10 cm dish	Greiner bio-one	664160

(*Continued on next page*)

Continued

REAGENT or RESOURCE	SOURCE	IDENTIFIER
0.22 μm filter	Millipore	SLGS033SS
Amilcon Ultra-15 10 k column	Millipore	UFC905024
48-well low adherence plate	Greiner bio-one	677970
Falcon™ Round-Bottom Polystyrene Test Tubes with Cell Strainer Snap Cap	Thermo Fisher Scientific	352235
Zeiss Axioskop2 Plus microscope	Carl Zeiss Microscopy, Jena, Germany	N/A
Zeiss AxioCam HRc digital camera	Carl Zeiss Microscopy, Jena, Germany	N/A
Four-laser Fortessa flow cytometer	Becton Dickinson	N/A
Leica TCS SP5 confocal microscope	Mannheim, Germany	N/A
Leica TCS SP8 confocal microscope	Mannheim, Germany	N/A
Inverted Leica SP8 Dive system (Leica, Mannheim, Germany) with an InSight X3 laser (Spectra –Physics)	Leica, Mannheim, Germany and Spectra –Physics	N/A
AxioscanZ1 microscope	Carl Zeiss Microscopy, Jena, Germany	N/A
Zeiss LSM 880 confocal microscope	Carl Zeiss Microscopy, Jena, Germany	N/A
CCD2-color microscope equipped with a Zeiss high resolution AxioCam 512 color camera	Carl Zeiss Microscopy, Jena, Germany	N/A
FACSAria Fusion	BD Biosciences	N/A

RESOURCE AVAILABILITY

Lead contact

Further information and request of resources and material can be directed to and will be fulfilled by the lead contact, Jacco van Rheenen (j.v.rheenen@nki.nl).

Materials availability

All unique reagents and models presented in this study are available upon request to the lead contact and will be subjected to a Material Transfer Agreement.

Data and code availability

Software used in this manuscript are listed in the key resources table. Data reported in this paper will be shared by the lead contact upon request. Any additional information to reanalyze the data reported in this paper is available from the lead contact. This paper does not report original code.

EXPERIMENTAL MODEL AND SUBJECT DETAILS

Animals

Animal experiments were performed at The Hubrecht Institute and the Netherlands Cancer Institute in accordance with national regulations and ethical guidelines. Experiments were approved by the Dutch Central Authority for Scientific Procedures on Animals (CCD) and the local animal experimental committees at The Hubrecht Institute and The Netherlands Cancer Institute. FVB/NRj females (Janvier) were used at 8–20 weeks of age and 18–23 grams at the time of intracranial, carotid injections or of isolation of the spleen. All mice were healthy, drug-naïve and did not undergo other procedures before intracranial or carotid injections or spleen isolation. Mice were randomized into experimental groups based on the IVIS signal measured in the BCBM. All mice were maintained in the Laboratory Animal Facilities of the Hubrecht and of the Netherlands Cancer Institute under specific pathogen free conditions. Mice were housed in individually ventilated cages, food and water were provided *ad libitum*.

Human samples

Human BCBM biospecimens were isolated at the University Medical Center of Leiden, the Netherlands. Before surgical removal of the BCBM, patients were informed and agreed about the use of their specimens for research. This opt-out procedure complies both with (inter-) national legislatives and ethical standards.

Primary tumor material digestion

For the first round of enrichment in the brain, primary breast tumors from MMTV-PyMT mice that carry an E-cadherin-mCFP transgene[36] and that had reached humane endpoint were harvested. Additionally, MMTV-Neu mice were crossed with E-Cad-mCFP mice

and primary breast tumors were also harvested when mice reached humane endpoint. Tumor pieces from breast tumors and from the rounds of enrichment were preserved in freezing medium (Thermo Fisher Scientific, Cat. No. 12648-010) at −80°C. Before intracranial injections, tumor pieces were thawed and minced on ice using sterile knives and enzymatically digested at 37°C for 20–30 min while shaking at 900 g. The digestion mix was composed of 10 mg collagenase A (Roche, Cat. No. 10103586001), 2 mL TrypLE Express (Thermo Fisher Scientific, Cat. No. 12605-010) and 3 mL DMEM/F12 GlutaMAX (Thermo Fisher Scientific, Cat. No. 10565018) supplemented with 10 mmol/L Hepes (Thermo Fisher Scientific, Cat. No. 15630106), 100 μg/mL streptomycin and 100 U/mL penicillin (Thermo Fisher Scientific, Cat. No. 15140122). Undigested tumor pieces were removed by spinning down at 800 g at 4°C and for 5 min. The pellet was treated with 10 μg/mL DNase I (Roche, Cat. No. 10104159001) in DMEM/F12 GlutaMAX medium and the tube was manually shaken for 5 min. The sample was washed three times in DMEM/F12 GlutaMAX and the final pellet was resuspended in 2 μL of phosphate-buffered saline (PBS) *per* intracranial injection. There was no *in vitro* culture step between rounds of enrichment in the brain.

Generation of the PyMT and Neu BCBM models

Tumor pieces derived from mammary tumors grown in MMTV-PyMT mice or in MMTV-Neu mice were digested as described in "Primary tumor material digestion" and intracranially injected. From the resulting tumor, we isolated tumor pieces and, after tumor digestion into single cells, we performed another round of intracranial injection. This *in vivo* selection was performed without any *in vitro* step in between rounds and for six successive rounds. Organoids from the last brain enrichment round were generated as described in "Organoids preparation, culturing and transduction".

Characterization of the PyMT BCBM model

Mice bearing PyMT BCBM generated by intracranial injections had an average survival latency of 4–5 weeks. Histopathological analyses demonstrated that PyMT BCBM derived from intracarotid injection are moderately to poorly differentiated adenocarcinomas with solid and/or lobular growth pattern and accompanied by thin fibrous vascular stroma and multifocal necrosis (Figure 1C). The tumor cells were round to polygonal in shape and had relatively large nuclei and conspicuous nucleoli. All these features resembled the human counterpart of BCBM (Figure 1C). Immunohistochemistry of markers that are not expressed in the brain, such as E-cadherin and pankeratin were strongly positive in PyMT BCBM and in human BCBMs while keratin 8/18 showed multifocal staining in PyMT BCBM and a strong staining in human BCBM (Figure S1B). In addition, GFAP, which is expressed in healthy brain tissue and in primary brain tumors but not in BM, was negative for both PyMT BCBM and human BCBMs (Figure S1B). Taken together, our mouse PyMT BCBM is comparable to human BCBMs in both histopathology and immunohistochemistry.

To further test whether our PyMT BCBM model mimics the human disease, we employed Magnetic Resonance Imaging (MRI) and performed T1-weighted post-contrast MRI of mice bearing a PyMT BCBM tumor (Figure S1B). Human BCBMs are characterized on MRI by well-defined tumor margins,[81] which was also observed in our mouse model (Figure S1C, solid arrow). In addition, we observed some heterogeneity within the tumor caused by the necrotic areas (in black, Figure S1C), which is often used in the clinic as an indication of high proliferation in the tumor.[81] Next, we employed the single-voxel PRESS technique[81] and acquired Magnetic Resonance Spectroscopy data from a volume of interest (VOI) of the contralateral healthy brain and the tumor (Figure S1D). In the tumor area, we observed a small decrease in the N-acetylaspartate (NAA) peak, a metabolite present in healthy neurons, which is typically decreased in human brain tumors.[81,82] An increase in the lactate + lipids peak was also detected in the tumor area compared to the contralateral healthy brain. Lactate is a marker of anaerobic metabolism occurring in fast proliferative tumors in human,[81] while the observed increase in the lipids peak is a result of cellular breakdown and consequent byproduct of necrosis. We observed in the tumor spectrum an increase in the choline peak compared to creatine, which is also found in human brain tumors and may be an indication of cellular proliferation and increased membrane turnover.[43]

Together, the mouse PyMT BCBM model displays key histological, MR imaging and MR spectroscopy characteristics of human BCBMs, and this warrants the use of our model to study this disease in pre-clinical settings.

Organoids preparation, culturing and transduction

From the last enrichment round in the brain, brain tumor pieces were isolated to generate tumor organoids. All steps were performed inside a flow cabinet and digestion was done as described in section "Primary tumor material digestion". Once the pellet was washed and spun down, it was resuspended in Basal Membrane Extract (BME) type 2 (R&D systems Cat. No. 3533-005-02) diluted at a 2:1 ratio with DMEM/F12 GlutaMAX medium (Thermo Fisher Scientific, Cat. No. 10565018). Drops of 50 μL of organoids with BME were platted in a pre-warm 24 well plate (Greiner bio-one, Cat. No. 662160) and inverted while solidifying for 30 min at 37°C, 5% CO_2. Organoids were maintained in complete DMEM/F12 GlutaMAX medium (Thermo Fisher Scientific, Cat. No. 10565018), supplemented with 10 mmol/L Hepes (Thermo Fisher Scientific, Cat. No. 15630106), 100 μg/mL streptomycin, 100 U/mL penicillin (Thermo Fisher Scientific, Cat. No. 15140122), 10.08 ng/mL FGF (Thermo Fisher Scientific, Cat. No. PHG0261) and B27 supplement (Thermo Fisher Scientific, Cat. No. 17504001) and incubated at 37°C, 5% CO_2. To confirm Mycoplasma-free culturing of the organoids, the MycoAlert PLUS Kit (Lonza Cat. No. LT07-118) was used according to the manufacturer's protocol. Additionally, organoids were tested for the presence of pathogens (*Corynebacterium bovis*, Corynebacterium sp. (HAC2), Ectromelia, EDIM, Hantaan, K virus, LCMV, LDEV, MAV1, MAV2, mCMV, MHV, MNV, Mouse kidney parvovirus (MKPV), MPV, MTV, MVM, *Mycoplasma pulmonis*, Mycoplasma sp., Polyoma, PVM, REO3, Sendai, TMEV) with IDEXX BioAnalytics (Kornwestheim, Germany). Organoids were split with TrypLE Express (Thermo

Fisher Scientific, Cat. No. 12605010) while shaking for 10–20 min at 900 g and 37°C. In order to visualize tumor cells *in vivo* we transduced these organoids with a lentiviral vector for stable expression of UBC-Firefly-Luciferase. Additionally, to visualize tumor cells in fluorescent assays, we transduced organoids with a construct for stable expression of UBC-H2B-Dendra2-puromycin. For production of the lentivirus, human embryonic kidney (HEK) 293T cells at a confluence of 80% were used. *Per* 10 cm dish (Greiner, Cat. No. 664160) of HEK 293T cells, 7.5 μg of psPAX2, 2.5 μg PMD2.G and 10 μg of the UBC-Firefly-Luciferase or UBC-H2B-Dendra2-puromycin constructs were mixed in 1 mL Opti-MEM (Thermo Fisher Scientific, Cat. No. 31985070). 1 mL of Opti-MEM with 40 μL lipofectamine 2000 (Thermo Fisher Scientific, Cat. No. 11668019) were added to the plasmid mix and incubated at room temperature for 15 min. The mix was carefully added to the HEK 293T cells and next morning medium was refreshed with DMEM GlutaMAX (Thermo Fisher Scientific, Cat. No. 31966047) supplemented with 100 μg/mL streptomycin, 100 U/mL penicillin (Thermo Fisher Scientific, Cat. No. 15140122). After 48 h, medium was collected and filtered through a 0.22 μm filter (Millipore, Cat. No. SLGS033SS). Filtered medium was concentrated with an Amilcon Ultra-15 10 k column (Millipore, Cat. No. UFC905024) for 1 h at 4,000 g. Organoids were trypsinized into smaller clusters of approximately 8 cells and incubated with 250 μL virus, 100 μg/mL polybrene (Sigma Aldrich, Cat. No. TR-1003-G) and 10 μmol/L Y-27632 (Bio Connect, Cat. No. S1049) on a 48-well plate low adherence (Greiner bio-one, Cat. No. 677970). Spin infection was done at 36°C, 600 g for 1 h and organoids were subsequently incubated at 37°C for 6 h. Next, organoids were washed twice with DMEM/F12 GlutaMAX medium (Thermo Fisher Scientific, Cat. No. 10565018) and plated in BME. Complete DMEM/F12 GlutaMAX medium (Thermo Fisher Scientific, Cat. No. 10565018), supplemented with 10 mmol/L Hepes (Thermo Fisher Scientific, Cat. No. 15630106), 100 μg/mL streptomycin, 100 U/mL penicillin (Thermo Fisher Scientific, Cat. No. 15140122), 10.08 ng/mL FGF (Thermo Fisher Scientific, Cat. No. PHG0261), B27 supplement (Thermo Fisher Scientific, Cat. No. 17504001) and 10 μmol/L Y-27632 (Bio Connect, Cat. No. S1049) was added to the organoids for 2 days. Organoids were selected with 0.5 μg/mL puromycin (Thermo Fisher Scientific Cat. No. A1113803).

Generation of BCBM cell lines

Cell lines were generated by trypsinizing the BCBM organoids with TrypLE Express (Thermo Fisher Scientific, Cat. No. 12605010) while shaking for 10–20 min at 37°C. Cells were plated in 2D on plastic-bottom plates and were cultured in DMEM, supplemented with 100 U/mL penicillin (Thermo Fisher Scientific, Cat. No. 15140122), streptomycin 10 mmol/L, FBS (10%, Thermo Fisher Scientific, Cat. No. A4766801), EGF (5 ng/mL, Thermo Fisher Scientific, Cat. No. 53003018) and Insulin (5 μg/mL, Sigma Aldrich, Cat. No. I0516) in 20% O_2, 5% CO_2 and at 37°C.

METHOD DETAILS

Intracranial injection

For intracranial surgeries, mice were treated with 0.067 mg/mL rimadyl (carprofen, Zoetis) in drinking water 1 day before injection and for 3 days following surgery. Furthermore, mice were treated with 0.1 mg/kg temgesic (buprenorphine, Indivior Europe Limited) via subcutaneous injection 30 min before and 8 h–12 h after surgery. Mice were anesthetized via inhalation of 2% (v/v) isoflurane and eyes were covered with duratears (Alcon). The head was shaved and disinfected using betadine. Scissors were used to make an incision in the skin over the cranium to reveal the periosteum, which subsequently was dissected away to reveal the bregma. Local anesthetic (0.01–0.02 mL) made of NaCl supplemented with 1 mg/mL Lidocaine (Fresenius Kabi) and 0.25 mg/mL Bupivacaine (Actavis, Aurobindo Pharma B.V.) was applied to the skull. The bregma was used as a 0 reference point to determine the position for intracranial injection: 1.5 mm to the right, 1.5 mm caudal and 1.5 mm deep. At this position a hole in the skull was drilled using a sterile compact drill bit. BCBM organoids expressing H2B-Dendra2 or Luciferase were dissociated into single cells with TrypLE Express (Thermo Fisher Scientific Cat. No. 12605010) at 37°C for approximately 10–20 min at 900 g until single cells were observed and were injected using a 10 μL glass Hamilton syringe with a 30G and point 4 style needle at a speed of 1 μL/min. *Per* mouse, 40,000 single cells derived from dissociated PyMT BCBM organoids and 50,000 single cells derived from dissociated Neu BCBM organoids in 2 μL were injected intracranially. We waited 2 min before retracting the needle to avoid spillage of cells outside the injection site. The wound was pressed with a sterile cotton tip and the skin was sutured. Mice were allowed to recover on a heating pad and closely monitored during the days following surgery.

Carotid injection

Similarly as for intracranial injection, PyMT BCBM organoids were collected and washed from the BME and digested with TrypLE Express (Thermo Fisher Scientific Cat. No. 12605010) at 37°C for 10–20 min at 900 g. Digestion was stopped by adding DMEM/F12 GlutaMAX medium (Thermo Fisher Scientific, Cat. No. 10565018) and organoids were dissolved in PBS and filtered through a Falcon™ Round-Bottom Polystyrene Test Tubes with Cell Strainer Snap Cap (Thermo Fisher Scientific, Cat. No. 352235). Mice were treated with 0.067 mg/mL rimadyl (carprofen, Zoetis) in the drinking water 1 day before injection and for 3 days post-surgery. Furthermore, mice were treated with 0.1 mg/kg temgesic (buprenorphine, Indivior Europe Limited) via subcutaneous injection 30 min before and 8 h–12 h after surgery. Mice were anesthetized via inhalation of 2% (v/v) isoflurane and eyes were covered with duratears (Alcon). Surgery was performed as described in Zhang et al.[83] The mouse was placed on a rubber plate and secured with rubber bands. The hair of the neck was shaved and the neck skin was cleaned with 70% ethanol. Subsequently, the mouse was placed on the stage of the dissecting microscope and a 1-cm long incision was made in the neck skin. The carotid

was exposed by dissecting the muscle, and the carotid was separated from the adjacent vagus nerve using surgical forceps. Next, the blood flow was blocked using surgical knots on the proximal end of the carotid. Cancer cells were subsequently injected and a surgical knot was tightened on the distal end of the carotid to complete the injection, prior to suturing the skin. *Per* mice, 10,000 PyMT BCBM single cells (made from dissociated PyMT BCBM organoids) were resuspended in 100 μL of PBS and were injected in the carotid. Mice were allowed to recover on a heating pad and closely monitored during the following days.

Immunohistochemistry

Mouse samples

Brain samples were collected and fixed in formalin or EAF (ethanol/acetic acid/formaldehyde/saline at 40:5:10:45 v/v/v/v) and embedded in paraffin. Sections were stained with hematoxylin and eosin (H&E) according to standard procedures. For immunohistochemistry, 4 μm-thick sections were made on which either E-cadherin (Cell Signaling, Cat. No. 3195, 1:100); Keratin 8 (DSHB University of Iowa, Troma 1, 1:1500); Glial Fibrillary Acidic Protein (GFAP) (BioTrend, Cat. No. BT46-5002-04, 1:500); Pankeratin (Thermo Fisher Scientific, Cat. No. MS-343-P, 1:100); CD4 (eBiosciences, Cat. No.14_9766_80, 1:2000); CD8 (eBiosciences, Cat. No. 14–0808, 1:1000); PD-1 (Cell Signaling, Cat. No. Cat. No. 84651, 1:1000); F4/80 (Cell Signaling, Cat. No. 70076, 1:1000); Ly6G (BD Biosciences, Cat. No. 551459, 1:500) and Foxp3 (eBiosciences Cat. No. 14–5773, 1:500) primary antibodies were applied. The sections were reviewed with a Zeiss Axioskop2 Plus microscope (Carl Zeiss Microscopy, Jena, Germany) and images were captured with a Zeiss AxioCam HRc digital camera and processed with AxioVision 4 software (both from Carl Zeiss Vision, München, Germany). For dual staining for CD4/CD44 and CD8/CD44, CD4 (eBiosciences, Cat. No.14_9766_80, 1:2000); CD8 (eBiosciences, Cat. No. 14–0808, 1:1000) were first applied and detected with a Goat-α-Rat-Biotynated secondary antibody (SouthernBiotech; 3052-08) which was revealed with an HRP visualization in NovaRed (Vector Laboratories; SK-4800). Next, CD44 (Santa Cruz, sc-18849, 1:100) was applied and detected with a Goat-α-Rat-Biotynated secondary antibody (SouthernBiotech; 3052-08) prior to being revealed with an AP visualization in blue (Vector Laboratories; SK-5300).

Human samples

Samples were fixed in 4% formaldehyde and embedded in paraffin. 4 μm-thick sections were stained with CD4 (Cell Marque, clone SP35), CD8 (Dako, clone C8/144B), PD1 (Dako, clone 22C3), GFAP (Dako, polyclonal (for Dako Omnis)), E-cadherin (Dako, clone NCH-38), pankeratin (Dako, clone AE1/AE3), Keratin 18 (Dako, clone DC10). The sections were reviewed with a Zeiss Axioskop2 Plus microscope (Carl Zeiss Microscopy, Jena, Germany) and images were captured with a Zeiss AxioCam HRc digital camera and processed with AxioVision 4 software (both from Carl Zeiss Vision, München, Germany).

In vitro drug treatment

BCBM organoids and cell lines were treated with 10 nmol/L (PyMT BCBM model) or with 20 nmol/L (Neu BCBM model) doxorubicin (Actavis) for 7 days, with a drug and medium renewal at day 4 after treatment initiation. PyMT BCBM organoids and cells, and mouse splenic T cells were treated with 10 μmol/L ABT263 (MedKoo, Cat. No. 201970) diluted in dimethyl sulfoxide (DMSO) for 48 h following pre-treatment with doxorubicin. The number of replicates performed for each *in vitro* treatment experiment is reported on the corresponding figure legend. No experiment was excluded.

In vivo drug treatment

Mice were intracranially injected with 40,000 cells obtained from dissociated PyMT BCBM organoids or with 50,000 cells from dissociated Neu BCBM organoids. Before initiation of treatment, mice were randomized based on IVIS total flux values into treatment groups. If mice did not develop a BCBM identified by IVIS 4 weeks after intracranial injection, they were excluded from the study. Timeline of treatment can be seen on the corresponding figures. The number of mice per treatment group is also reported in the corresponding figure legend.

Saline vehicle (control for doxorubicin): three times every 5 days, same volume of saline as doxorubicin, administered via intravenous injection.

Doxorubicin treatment: For doxorubicin pre-treatment, mice were treated three times every 5 days with doxorubicin (Actavis, 5 mg/kg) administered via intravenous injection. For continuous treatment, mice were also treated once weekly on day 1 with doxorubicin (Actavis, 5 mg/kg) administered via intravenous injection until reaching humane endpoint.

IgG treatment: As controls for depletion of T cells, on days 1, 3 and 5 prior to treatment with vehicle or with chemotherapy, mice were treated with 400 μg (day 1) or 200 μg (day 3 and day 5) with *InVivo*MAb rat IgG2b isotype control (BioXCell, clone LTF-2, Cat. No. BE0090). As controls for anti-PD1 treatment, mice were treated twice weekly with 400 μg (day 1) and 200 μg (day 4) with *InVivo*MAb rat IgG2b isotype control (BioXCell, clone 2A3, Cat. No. BE0089). Both IgG controls were administered by intraperitoneal injection.

anti-CD4 treatment: on days 1, 3 and 5 prior to treatment with vehicle or with chemotherapy, mice were treated with 400 μg (day 1) or 200 μg (day 3 and day 5) with *InVivo*MAb anti-mouse CD4 (BioXCell, clone GK1.5, Cat. No. BE003-1) which was administered by intraperitoneal injection.

anti-CD8 treatment: on days 1, 3 and 5 prior to treatment with vehicle or with chemotherapy, mice were treated with 400 μg (day 1) or 200 μg (day 3 and day 5) with *InVivo*MAb anti-mouse CD8 (BioXCell, clone YTS 169.4, Cat. No. BP0117) and administered by intraperitoneal injection.

anti-PD1 treatment: mice were treated twice weekly with 400 μg (day 1) or 200 μg (day 4) of *InVivo*MAb anti-mouse PD1 (BioXCell, clone RMP1-14, Cat. No. BE0146) which was administered by intraperitoneal injection.

Cremophore EL vehicle: As a control for ABT263 treatment, mice were treated every second days, for 7 days, with a cremophore EL vehicle (DMSO:Cremophore EL:saline as 1:1:8 (v:v:v)) and with the same volume as ABT263, by oral gavage.

ABT263 treatment: mice were treated every second days, for 7 days, with 50 mg/kg of ABT263 (Medkoo, Cat. No. 201970) by oral gavage.

We want to disclaim that we observed that treatment with doxorubicin and with doxorubicin and anti-PD1 triggered toxicity such as weight loss and paleness in some mice. Therefore, we found that 2/8 mice with PyMT BCBM and 3/8 mice with Neu BCBM treated with doxorubicin followed by anti-PD1 (Figures 5 and 7D) had a smaller tumor when sacrificed compared to mice receiving monotherapies, suggesting that the anti-tumor effects of the combination therapy are actually larger than the survival data shown in Figures 5 and 7.

Flow cytometry analysis of immune panels

BCBM were dissociated into single-cell suspensions using a Brain Tumor Dissociation kit (Miltenyi Biotec, Cat. No. 130-095-942) and according to the manufacturer's instructions. Subsequently, samples were blocked in FACS buffer containing 1:50 Fc block CD16/CD32 (BD Biosciences, Clone 2.4G2, Cat. No. 553141) for 20 min at room temperature, and then stained with antibodies (see details in Figure S3 and key resources table). Samples were permeabilized and fixed with a fixation and permeabilization kit (Thermo Fisher Scientific, Cat. No. 00-5523-00), according to the manufacturer's protocol, and then stained with intracellular antibodies (see details in Figure S3 and key resources table). Signals were detected on a four-laser Fortessa flow cytometer (Becton Dickinson) and analyses were performed with FlowJo software, with the gating strategy presented in Figure S3. We did not exclude any sample from the analysis.

IVIS imaging

Bioluminescence imaging was performed with an IVIS200 camera (PerkinElmer; Waltham, MA USA) 10 min after intraperitoneal injection of 150 mg/kg Beetle Luciferin (Promega, Cat. No. E1605). Mice were anesthetized with 2% (v/v) isoflurane prior and during imaging. Signal flux was obtained using open filters and high binning for mice injected in the carotid (Figures 1B, S1A, and S1B), and with small binning for mice bearing BCBM derived from intracranial injections (Figure 5).

Magnetic resonance imaging

Magnetic resonance imaging was performed with a 7 Tesla BioSpec 70/20 USR (Bruker; Billerica, MA USA). Figure 1B was imaged with a T2 RARE sequence with a 3.9 ms echo-time, 2200 ms repetition time and 8 averages. Figures S1C and S1D was imaged with a T1-weighted post-contrast sequence with a 3 ms echo-time, 235 ms repetition time and a flip angle of 30°. PRESS sequence was performed with a 17 ms echo-time, 2500 ms repetition time, 256 averages and a volume-of-interest of 1.8 × 1.8 × 1.8 mm size. Paravision software (v6.0.1; Bruker) was used for image acquisition. The contrast agent used was Gadoterate meglumine (Dotarem®; 0.5 mmol/mL; Guerbet; Villepinte, France) diluted 5 times with saline and injected intravenously through a cannula via tail vein. Mice were anesthetized with 2% (v/v) isoflurane during imaging and the heart rate was monitored throughout the procedure.

Immunofluorescence and microscopy

For organoids: organoids were fixed in 4% paraformaldehyde for 20 min at room temperature, followed by permeabilization in 0.2% TritonX-100 in PBS for 15 min at room temperature. A block was next performed in 5% bovine serum albumin (BSA) diluted in PBS (wt:v) for 2 h at room temperature, followed by staining overnight at 4°C with anti-Cleaved Caspase 3 (1:400, Asp175, Cell Signaling, Cat. No. 9661). Appropriate Alexa Fluor labeled secondary antibody (Thermo Fisher Scientific) was combined with DAPI (1 μg/mL) and incubated for 2 h in the dark at room temperature.

For BCBM sections: samples were fixed in a PLP buffer containing 1% paraformaldehyde, 0.2% $NaIO_4$, 37.5% L-lysine and 37.5% P-buffer (containing 81% of Na_2HPO_4, 19% of NaH_2PO_4 diluted in water, pH = 7.4) for 24 h at 4°C. Subsequently, samples were moved to a sucrose solution for 12 h, at 4°C, prior to being embedded in OCT Tissue Tek (Thermo Fischer Scientific, Cat. No. 11381785) and stored at −80°C.

5 μm sections were rehydrated in PBS for 10 min at room temperature. Samples were subsequently permeabilized and blocked for 30 min at room temperature in a buffer made of 5% normal goat serum in PBS (v:v), 2.5% BSA in PBS (wt:v) and 0.5% Triton X-100 (v:v) diluted in PBS. Samples were washed twice in PBS containing 3% BSA, prior to incubation with antibodies against T cells (anti-mouse CD4-eFluor660, 1:200; eBioscience, clone GK1.5, Cat. No. 50-0041-82; anti-mouse CD8-eFluor660, 1:200, eBioscience, clone 53-6.7, Cat. No. 50-0081-82; anti-mouse CD31, 1:100, BD Biosciences, clone MEC 13.3, Cat. No. 550274; anti-mouse VCAM-1/CD106, 1:100, R&D Systems, Cat. No. AF643-SP; anti-mouse ICAM/CD54, 1:100 R&D Systems AF796-SP, anti-mouse NG2 Chondroitin Sulfate Proteoglycan (1:250, Millipore, Cat. No. AB5320) or anti-α-smooth muscle actin (1:100, Sigma-Adrich, Cat. No. A5228) at 4°C overnight. Samples were then washed three times in PBS and incubated for 5 min at room temperature with DAPI (0.1 μg/mL) in the dark. Slides were washed three times in PBS and mounted with Vectashield hard set (Vectorlab, Cat. No. H-1400-10).

For organoids, images were acquired on an inverted Leica TCS SP5 confocal microscope (Mannheim, Germany), in 8 bit with a 20× objective. Fiji was used for quantification. Quantification of cleaved-caspase 3 staining was performed as follows: the number of cleaved-caspase 3 positive cells was quantified in 3 representative fields of view *per* replicate and was counted as a percentage of all ($DAPI^+$) cells. The experiment was performed in 5 biological repeats (PyMT BCBM) and in 3 biological repeats (Neu BCBM). Each dot presented on the graphs represents the averaged value of the percentage of cleaved-caspase 3^+ cells *per* biological repeat. We did not exclude any repeats.

For slides stained with anti-CD4 and anti-CD8 antibodies, images were acquired on an inverted Leica TCS SP5 confocal microscope (Mannheim, Germany), in 8 bit with a 20× objective. For slides stained with cleaved-caspase 3, images were acquired on an inverted Leica TCS SP8 confocal microscope (Manheim, Germany) in 8 bit with a 40× objective. The number of samples imaged and analyzed is reported in the corresponding figure legends. We did not exclude mice.

For slides stained with CD31, ICAM, VCAM, NG2 and α-smooth muscle actin, slides were scanned on an AxioscanZ1 microscope (Carl Zeiss Microscopy, Jena, Germany) in 8 bit with a 20× objective. Images were deconvoluted and stitched in Huygens software and converted to a 16 bit format in Fiji. Using Imaris, $CD31^+$ vessels present inside the BCBM ($H2B\text{-}Dendra^+$ area) were segmented and staining intensity of VCAM, ICAM and α-smooth muscle actin were quantified inside the segmented vessels. Intensity of NG2 was quantified in the vicinity (0–10 μm) of the segmented vessels. Data were normalized to the area covered by $CD31^+$ vessels in each BCBM. The number of samples imaged and analyzed is reported in the corresponding figure legends. We did not exclude mice.

For staining for Lamin B1, 5 μm sections were dried for 15 min at room temperature, rehydrated in PBS for 10 min at room temperature and permeabilized and blocked for 30 min at room temperature in a buffer made of 2.5% (v/v) normal goat serum, 1% (wt/v) BSA and 0.1% (v/v) Triton X-100 diluted in PBS. Samples were washed twice in PBS containing 1% (wt/v) BSA, prior to incubation with the antibody against Lamin B1 (1:500, Abcam, clone GR3244890-2, Cat. No. ab16048) for 2 h at room temperature. Samples were then washed twice in PBS containing 1% BSA and incubated for 1 h at room temperature with appropriate secondary antibody and Hoechst 33342 (5 μg/mL, Thermo Fischer, Cat. No. H3570) in the dark. Slides were washed three times in PBS, once in water and mounted with hard set ProLong Glass Antifade Mountant (Thermo Fischer, Cat. No. P3680). Images were acquired on a Zeiss LSM 880 confocal microscope (Carl Zeiss Microscopy, Jena, Germany), in 16 bit with a 40× objective. Fiji was used for quantification. The number of samples imaged and analyzed is reported in the corresponding figure legends. We did not exclude mice.

Flow cytometry analysis of cell apoptosis

Cell death was analyzed by quantification of cells positive for the death marker 7-AAD. Organoids were collected and dissociated into single cells by incubating them in TrypLE Express (Thermo Fisher Scientific Cat. No. 12605010) at 37°C for approximately 20 min at 900 g. The cell suspension was filtered on a cell strainer and incubated with 7-AAD dye (Biolegend, Cat. No. 420404) for 10 min, on ice in the dark. Samples were processed on a Fortessa flow cytometer (Becton Dickinson) and analyses were performed with FlowJo software. This experiment was performed in three biological repeats. We did not exclude any repeat.

SA β-Galactosidase activity in tissue sections

SA β-galactosidase staining was performed on 5 μm-thick cryo-sections of BCBM tumors using a commercial kit (Sigma Aldrich, Cat. No. 11828673001) and according to the manufacturer's instructions. SA β-galactosidase activity was quantified by manually counting the number of $SA\text{-}β\text{-}galactosidase^+$ cells *per* field of view, as depicted in the figures. *Per* tumor, 5 FOV were quantified. Data depicted on the graphs are averaged values of all FOV *per* mouse.

SA β-Galactosidase activity *in vitro*

200,000 cells were seeded in 6-well plates and treated with PBS or with doxorubicin 10 nmol/L (PyMT BCBM) or doxorubicin 20 nmol/L (Neu BCBM model) for 7 days. Cells were passaged once in the PBS condition over this 7-day period. Next, for the PyMT BCBM model, medium was renewed and cells were treated with DMSO or with ABT263 10 μmol/L for 48 h. Cells were subsequently stained using the Senescence Cells Histochemical Staining Kit (Sigma-Aldrich, Cat. No. CS0030) according to the manufacturer's instructions. Cells were imaged on a bright field CCD2-color microscope equipped with a Zeiss high resolution AxioCam 512 color camera (Carl Zeiss Microscopy, Jena, Germany). The total number of cells and the $SA\text{-}β\text{-}galactosidase^+$ cells were counted from 5 representative fields of view *per* condition.

RT-qPCR

RNA samples were isolated using Trizol (Invitrogen Life Technology, Cat. No. 15596018), according to the manufacturer's protocol and stored at −80°C. Complementary DNA was synthesized using 1 μg of RNA *per* sample and with the High Capacity cDNA Reverse Transcription kit (Thermo Fischer Scientific, Cat. No. 4368814), according to the manufacturer's protocol. Reverse transcription was performed in a PCR machine following these steps: 10 min at 25°C, 120 min at 37°C and 5 min at 85°C. qPCR was performed using Power SYBR Green PCR Master Mix (Thermo Fischer Scientific, Cat. No. A25777) in a QuantStudio Real-Time qPCR machine. Thermal cycle conditions were as follows: 2 min at 50°C, 2 min at 95°C followed by 45 cycles consisting of denaturation for 15 s at 95°C, annealing for 1 min at 60°C, and extension for 1 min at 72°C. PCR reactions were concluded with incubation for 10 min at 72°C. Relative values were quantified using the ddCt method and mean values were plotted with SEM. Sequences of primers used in this study are as follows: *FOX O 4*: forward: TCTACGAATGGATGGTCCGCAC, reverse: CTTGCTGTGCAAGGACAGGTTG;

CDKN2A: forward: TGTTGAGGCTAGAGAGGATCTTG, reverse: CGAATCTGCACCGTAGTTGAGC; *Ki67*: forward: CTGCCTGCGAA GAGAGCATC, reverse: AGCTCCACTTCGCCTTTTGG; *GAPDH*: forward: GGGTTCCTATAAATACGGACTGC, reverse: CCATTTTG TCTACGGGACGA.

Effects of ABT263 on T cells

Ki67-assessment

Splenocytes were isolated from tumor naive, untreated FVB/NRj female mice and cultured in Roswell Park Memorial Institute (RPMI) 1640 Medium (Thermo Fisher Scientific, Cat. No. 21875034) containing FBS (10%, Thermo Fisher Scientific, Cat. No. A4766801), Penicillin/streptomycin (10,000 U/mL; Thermo Fisher Scientific, Cat. No. 15140-122), IL2 (10 U/mL, Thermo Fisher Scientific, Cat. No. PMC0025), β-mercaptoethanol (50 μmol/L), Ultraglutamine (2 mmol/L, Lonza, Cat. No. BE17-605E/U1), PMA (50 ng/mL, Sigma Aldrich), ionomycin (1 μg/mL, Sigma Aldrich), in plate pre-coated with anti-CD3 (1 μg/mL, BD Bioscience, clone 17A2, Cat. No. 564008). Splenocytes were cultured in the presence of DMSO or ABT263 (10 μmol/L) for 48 h. Next, splenocytes were washed twice in FACS buffer and were blocked for 5 min at room temperature in a blocking buffer (FACS buffer containing 1:50 Fc block CD16/CD32 (BD Biosciences, Clone 2.4G2, Cat. No. 553141)) prior to staining with an anti-CD3 antibody (BD Bioscience, clone 17A2, Cat. No. 564008, 1:100). Next, splenocytes were incubated with DAPI (1 μg/mL) and permeabilized in a Foxp3 fixation/permeabilization buffer (eBioscience, Cat. No. 00-5523-00) for 30 min, in the dark and at 4°C. Cells were washed twice in permeabilization buffer (eBioscience, Cat. No. 00-8333-56), blocked for 5 min in FACS buffer containing 1:50 Fc block and stained with an anti-Ki67 AF647 antibody (1:100, BD Pharmigen, Cat. No. 558615). Splenocytes were analyzed on a Fortessa flow cytometer Becton Dickinson) and analyses were performed with FlowJo software. This experiment was performed in three biological repeats and we did not exclude any repeat.

Assessment of T cell migration

T cells were isolated by flow cytometry from the spleen of tumor naive, untreated ROSA26^{mTmG} FVB/NRj female mice. Spleens were gently mechanically dissociated using a scalpel blade and glass slides and single cells were incubated in a red cell lysis buffer (NH4Cl 155 mmol/L, KHCO3 1 mmol/L, 0.1 mmol/L EDTA diluted in MilliQ water, pH = 7.4) for 5 min at room temperature. Next, splenocytes were blocked for 5 min at room temperature in a blocking buffer (FACS buffer containing 1:50 Fc block CD16/CD32 (BD Biosciences, Clone 2.4G2, Cat. No. 553141)) and incubated with primary antibodies in the dark for 45 min at 4°C (anti-CD11b-BV650 (1:1200, Biolegend, clone M1/70, Cat. No. 101259); anti-CD4-eFluor660 (1:300, BD Bioscience, clone GK1.5, Cat. No. 50-0041-82); anti-CD8-eFluor660 (1:100, ThermoFisher, clone 53-6.7, Cat. No. 50-0081-82). Samples were sorted on a Fusion Cell Sorter, DAPI^{+} (dead cells) and CD11b^{+} cells (myeloid cells) were excluded and T cells were isolated based on CD4/CD8 expression. Following isolation, T cells were cultured in plates coated with an anti-CD3 antibody (1 μg/mL, BD Bioscience, clone 17A2, Cat. No. 564008) in RPMI 1640 Medium (Thermo Fisher Scientific, Cat. No. 21875034) containing FBS (10%, Thermo Fisher Scientific, Cat. No. A4766801), Penicillin/streptomycin (10,000 U/mL; Thermo Fisher Scientific, Cat. No. 15140-122), IL2 (10 U/mL, Thermo Fisher Scientific, Cat. No. PMC0025), β-mercaptoethanol (50 μmol/L), Ultraglutamine (2 mmol/L, Lonza, Cat. No. BE17-605E/U1), PMA (50 ng/mL, Sigma Aldrich), ionomycin (1 μg/mL, Sigm aAldrich). T cells were treated with DMSO or ABT263 (10 μmol/L) for 48 h. Subsequently, T cells were embedded in a mix of BME and T cell medium (1:1 ratio) and plated in a glass-bottom chamber. T cells were imaged on an inverted Leica SP8 Dive system (Leica, Mannheim, Germany) with an InSight X3 laser (Spectra –Physics). ROSA26^{mTmG} was excited with 960 nm (Insight X3) and detected at 564–698 nm (HyD-RLD4). Time-lapse movies were acquired with a 5 μm z-step and imaged every 10 min for a total of 5 or 6 h. All images were acquired in 12 bit and with a 25×/0.95 NA water immersion objective. T cell migration was analyzed in Imaris using the spot function. This experiment was performed in four biological repeats, we excluded one repeat where we did not observe any T cell movement in neither condition.

QUANTIFICATION AND STATISTICAL ANALYSIS

Unless mentioned otherwise in the figure legends, p-values were determined by unpaired, nonparametric t test with a Mann-Whitney *U* correction in Prism (GraphPad). Kaplan Meier survival curves were analyzed with a log-rank Mantel-Cox test. Exact p-values are reported on each graph of the figures of this manuscript. 'n' reports the number of technical and biological repeats as well as the number of mice on the corresponding figure legends and, where appropriate, in the relevant sections of the 'method details' of the STAR Methods. Unless specified otherwise in the figure legend, data are presented as mean with SEM. Mice that did not develop BCBM within 4 weeks of intracranial injections were excluded from the analysis. Image analysis and quantification are described in the relevant sections of the "method details" of the STAR Methods.